For typeset version:

Lipiejko, N., Jones, T.J., Penner, J. (2026). Shear cell measurements of the internal and basal friction angles of pyroclastic material: implications for pyroclastic density currents. 108605. *Journal of Volcanology and Geothermal Research.*

https://doi.org/10.1016/j.jvolgeores.2026.108605

Highlights

Shear cell measurements of internal and basal friction angles of pyroclastic material: implications for pyroclastic density currents

Natalia Lipiejko, Thomas J. Jones, Julia Penner

- Friction angles of volcanic material were studied through shear cell measurements
- Three internal friction angles and wall friction angle are reported
- The impact of friction on flow dynamics are discussed through Titan2D simulations

Shear cell measurements of internal and basal friction angles of pyroclastic material: implications for pyroclastic density currents

Natalia Lipiejko[a], Thomas J. Jones[a], Julia Penner[a]

[a]*Lancaster Environment Centre, Lancaster University, Library Avenue, Bailrigg, Lancaster, LA1 4YQ, United Kingdom*

Abstract

Geophysical granular flows such as pyroclastic density currents, debris flows, and avalanches are mixtures of fluid and solid particles which propagate at great velocities and distances away from the source. The dynamics of granular flows are governed by parameters such as the physical properties of the individual particles, the particle-particle interactions, as well as the interactions between the flow and the environment. Given the devastating nature of geophysical granular flows, it is crucial to accurately model their flow path and runout distance. Granular flows have often been described using depth-averaged equations and form the basis of many geophysical numerical models that unpin hazard maps. The main input parameters for such models are the frictional properties of the granular flow, specifically the internal friction angle and the bed ($\sim$wall) friction angle. This study presents an experimental investigation into both the internal and the wall friction angles of natural pyroclastic material of particle diameter $< 710\,\mu$m. The internal friction angles were measured for a range of pre-shear (consolidating) stresses, $\sigma_p =$ 1.5-9 kPa. The wall friction angle was measured between the pyroclastic material and sandpaper with the particle size to the sandpaper particle size ratio, i.e., roughness, $d_{50}/d_s = 0.07$ - 3.90 for $\sigma_p =$ 1.5-9 kPa. The internal friction angle, the effective internal friction angle, the internal friction angle at a steady-state flow, and the wall friction angles are all reported. The importance of these angles for the flow dynamics is illustrated through Titan2D simulations of a granular flow travelling down an idealised volcano.

Keywords: pyroclastic density currents, internal friction angle, wall friction angle, shear cell, granular material, depth-averaged model

1. Introduction

Granular gravity currents are mixtures of fluid and solid particles which propagate in an ambient fluid and are driven by the density difference between the current and the ambient environment. Geophysical granular currents such as pyroclastic density currents, debris flows, landslides, and snow avalanches are a common occurrence on the Earth's surface and pose significant hazards to the populations and infrastructures. The dynamics of such granular flows depend on parameters such as the size, shape, and density of individual particles, the ambient fluid density, substrate physical properties, as well as the particle-particle, particle-fluid, and particle-substrate interactions. There have been numerous studies investigating the complex physical processes governing geophysical granular flows with the overarching aim of forecasting both the flow path and runout distance, which in turn informs hazard and risk mitigation strategies (Savage and Hutter, 1991; Iverson and Denlinger, 2001; Dartevelle, 2004; Hutter, 2005; Forterre and Pouliquen, 2008; Delannay et al., 2017; Lube et al., 2020; Jones et al., 2023).

One of the common models used for a granular flow propagating down a slope is a depth-averaged model (also known as a shallow-water or Saint-Venant model) which assumes that the flow is incompressible and thin compared to its down-slope extent (i.e., small aspect ratio) (Savage and Hutter, 1991; Delannay et al., 2017). The model also assumes a Coulomb (1776) friction which relates the shear stress, τ to the normal stress, σ through the bed (also known as basal) friction angle, φ_{bed}

$$\tau = \sigma \tan \varphi_{bed} + c, \tag{1}$$

where φ_{bed} is the bed (also known as basal) friction angle - an angle that a plane needs to be inclined at for the granular material to move downslope at a constant speed - and c is the cohesion. The mass and momentum conservation equations are averaged over the flow depth and the resulting system contains three unknowns, the thickness and the two mean (depth-averaged) velocity components of the granular flow. For a granular flow travelling down a plane inclined at θ, the depth-averaged mass and momentum conservation equations are

$$\frac{\partial h}{\partial t} + \frac{\partial (hu)}{\partial x} + \frac{\partial (hv)}{\partial y} = 0 \tag{2}$$

$$\frac{\partial (hu)}{\partial t} + \frac{\partial (hu^2)}{\partial x} + \frac{\partial (huv)}{\partial y} = gh \sin\theta_x - \frac{1}{2} k_{act/pass} \frac{\partial (gh^2 \cos\theta)}{\partial x} + \tau_x \tag{3}$$

$$\frac{\partial (hv)}{\partial t} + \frac{\partial (hvu)}{\partial x} + \frac{\partial (hv^2)}{\partial y} = gh \sin\theta_y - \frac{1}{2} k_{act/pass} \frac{\partial (gh^2 \cos\theta)}{\partial y} + \tau_y, \tag{4}$$

where g is the gravitational acceleration, $h(x, y, t)$ is the thickness of the flow perpendicular to the local slope, u and v are the depth-averaged velocities parallel to the local bed surface in the x and y direction, respectively, and define the velocity vector $\mathbf{u} = (u, v)$. $\tau = (\tau_x, \tau_y)$ is the retarding stress opposing flow with τ_x and τ_y corresponding to the stresses in the x and y direction, respectively. The parameter $k_{act/pass}$ is the lateral stress coefficient (also known as the Earth's pressure coefficient), and is the ratio of bed-parallel to bed-normal stress (Savage and Hutter, 1991). The parameter $k_{act/pass}$ is derived assuming Coulomb (1776) model of rate-independent frictional behaviour in diverse granular media and it is defined by Iverson and Denlinger (2001) as

$$k_{actpass} = 2\frac{1 \pm [1 - \cos^2\varphi_{int}(1 + \tan^2\varphi_{bed})]^{1/2}}{\cos^2\varphi_{int}} - 1, \tag{5}$$

where φ_{int} is the internal friction angle, and ± is positive for a converging flow (k_{pass}) and negative for a diverging flow (k_{act}). A converging flow corresponds to a flow where the fluid propagates through a constriction, for example, water flowing from a wide pipe to a pipe of a smaller cross-sectional area. The change in area leads to an increase in the flow velocity ($\partial u/\partial x + \partial v/\partial y < 0$). Conversely, a diverging flow describes a situation where the flow path becomes wider, for example, a wider path of a river, resulting in a decrease in the flow velocity ($\partial u/\partial x + \partial v/\partial y > 0$). In general, the angle of internal friction, φ_{int} is a result of solid particles flowing against each other. Both angles are described fully within Section 2.

The depth-averaged model has been the framework for several geophysical numerical models, for example, VolcFlow (Kelfoun and Druitt, 2005), TITAN2D (Patra et al., 2005), D-Claw (Iverson and George, 2014), and IMEX_SfloW2D (de' Michieli Vitturi et al., 2019, 2023). These models are widely used by researchers, volcano observatories, risk and disaster advisory centres, and governmental institutions for simulating pyroclastic density currents, lahars, debris flows, landslides, avalanches, and many other geophysical granular flows (e.g., Williams et al., 2008; Procter et al., 2010; Sheridan et al., 2010; Alcozer-Vargas et al., 2022; Azzaro et al., 2023; Aydar et al., 2025). Given that the resulting simulations may be used to help mitigate against the hazards posed by geophysical flows, it is of utmost importance that the simulations are as accurate as possible (Cui et al., 2025). Equations 1-5 highlight the importance of understanding the properties of the granular flow (φ_{int}) and the terrain (i.e., the substrate/bed) it is travelling on (φ_{bed}) for physically accurate modelling of the flow dynamics. In this study, we present an experimental investigation into the internal and the wall friction angles of natural pyroclastic material, where the wall friction angle, φ_{wall} is the interface friction angle between the material and a prepared surface. For geophysical flows, the bed friction angle and the wall friction angle refer to the same quantity in the basal boundary condition. To relate our laboratory measurements to the physical properties of natural flows, we first provide an in-depth introduction to the properties of granular materials and associated analysis of laboratory data in Section 2, followed by the description of the experimental methodology in Section 3. Section 4 presents the analysis of the experimental data, i.e., the calculated friction angles, the impacts of which are illustrated in Section 5 through Titan2D simulations of a granular flow travelling down an idealised volcanic cone. Finally, the limitations of this study are discussed in Section 6.

2. Properties of granular materials

When an elastic solid is subjected to an external force acting along a plane α, it will deform elastically (Figure 1a). The resulting shear strain, γ can be related to the applied shear stress τ by a constitutive relationship of the form

$$\tau = f(\gamma). \tag{6}$$

In the case of viscous Newtonian fluids, this relationship takes the well known linear form of $\tau = \mu_f \gamma$, where μ_f is the fluid viscosity (Nedderman, 1992; Whorlow, 1992; Mader et al., 2013). When a bulk solid, i.e., granular material, is subjected to an external force acting along a plane α, it will deform elastically for small values of force. However, when the force reaches a critical value, the granular material divides itself into two parts which slide past each other along a plane inclined at an angle α (Figure 1a-b). This is called a rigid-plastic failure mode, where the granular material is assumed to divide itself into two rigid parts which slide over a narrow plastic zone, also known as the yield, slip, or failure plane (Nedderman, 1992). The shear stress acting on the slip plane can be related to the normal stress by a constitutive relationship of the form

$$\tau = f(\sigma). \tag{7}$$

Materials for which this equation takes the form of Equation 1 are known as ideal Coulomb materials (Coulomb, 1776; Iverson and Denlinger, 2001). If the shear stress $\tau < \sigma \tan \varphi_{bed} + c$, the force acting on the bulk solid is not sufficiently large, and the bulk solid remains undisturbed. If $\tau = \sigma \tan \varphi_{bed} + c$, a slip plane will be generated and the bulk solid will experience rigid-plastic failure (Nedderman, 1992; Pouliquen, 2025).

Figure 1c shows the shear and normal stresses on a two-dimensional element of a bulk solid that is subject to a force acting along a plane inclined at an angle α. The stresses acting on the x-plane are $\sigma_{xx} \cos \alpha$ and $\tau_{xy} \cos \alpha$ and the stresses on the y-plane are $\sigma_{yy} \sin \alpha$ and $\tau_{yx} \sin \alpha$. As a convention, compressive stresses are considered as positive, and shear stresses are taken as positive when acting on an element in an anticlockwise direction. Such stresses can be analysed using a method called Mohr's circles and are plotted in a σ-τ diagram in Figure 1d (Jenike and Shield, 1959; Jenike, 1976; Schulze, 2014; Pouliquen, 2025). The centre of the circle is located at

$$(\sigma, \tau) = \left(\frac{\sigma_{yy} + \sigma_{xx}}{2}, 0 \right) \tag{8}$$

and the radius of the circle is

$$R = \frac{\sigma_{yy} - \sigma_{xx}}{2}. \tag{9}$$

The Mohr stress circle thus represents the stresses on all slip planes at an arbitrary inclination angle α, i.e., on all possible slip planes within a bulk solid element. The centre of the Mohr stress circle is always located on the σ-axis ($\tau = 0$), therefore each Mohr stress circle has two points of intersection with the σ-axis which define the normal stresses, also known as the principal stresses. The larger principal stress, σ_1 is called the major principal stress and the smaller principal stress, σ_2 is called the minor principal stress (Jenike and Shield, 1959; Jenike, 1976; Nedderman, 1992; Schulze, 2014).

The internal properties of a bulk solid can be measured through shear cell testing, as shown in Figure 1e. Frequently used tests include a direct translational (Jenike) test and a rotational test (Jenike and Shield, 1959; Schulze, 2014). Shear testing equipment includes a bottom cell for the granular material and the upper part to confine and shear the sample. In the Jenike shear tester, the upper part is moved vertically downwards to compress the sample at a pre-selected normal stress, then, it is displaced horizontally against the fixed bottom cell. The normal stress, σ, and the shear stress, τ are measured. Although the Jenike Shear Tester is internationally recognised, its main disadvantages include long test durations and large errors associated with manual preparation of each measured sample (Schulze, 2014).

A rotational shear test is performed in a shear cell (Figure 1f), where the granular material is compressed at a pre-selected normal stress σ and sheared at a constant rotation rate while the shear stress, τ is measured. A standard, internationally accepted (Schulze, 2014; ASTM International, 2015) shear test procedure exists and is detailed here as follows (Figure 1g). In order to measure the internal friction at a given pre-shear normal stress, the granular material is consolidated at the pre-selected value of pre-shear normal stress, σ_p (also known as a consolidating stress) before the measurement. Following this, the shearing test is initiated which measures the maximum shear stress, τ, as a response to the pre-selected normal stress, σ at the prescribed pre-shear normal stress, σ_p. The material is sheared at a constant rotation rate while maintaining σ until a maximum shear stress, τ is achieved and τ has subsequently reduced (incipient flow or failure point). This routine is typically performed for five measuring points, i.e., five pre-selected values of σ which are between 20% and 80% of σ_p.

These shear test data enable calculations of the angle of internal friction, φ_{int}, the effective angle of internal friction, φ_{eff}, and the angle of internal friction at a steady-state flow, φ_{ss} (Jenike, 1976; Nedderman, 1992; Schulze, 2014). The data analysis starts with plotting the shear test points and the pre-shear point (the pre-shear normal stress, σ_p and the measured pre-shear shear stress, τ_p) on a σ-τ diagram (Figure 1g). The angle of internal friction, φ_{int} is the slope of the line going through all the shear test points (but not the pre-shear point). This line is called the yield locus. The intercept of the yield locus with the τ-axis is the cohesion of the granular material. The effective angle of internal friction, φ_{eff} informs about the internal friction during the flow of the granular material and forms the basis of a conventional silo design, for example (Jenike, 1976). This angle is a slope of the line crossing through the origin and tangent to the greater Mohr's circle (steady-state flow circle; black Mohr's circle in Figure 1g). This line is called the effective yield locus. The greater Mohr's circle is constructed such that it crosses through the pre-shear point and its origin and radius are calculated using Equations 8 and 9, respectively. Finally, the angle of internal friction at a steady-state flow, φ_{ss} is the slope of the line crossing through the origin and the pre-shear point. This angle is the measure of the internal friction of granular material at a steady-state flow, i.e., when it is consolidated at σ_p. The angle φ_{ss} is the angle used for the previously discussed depth averaged models of geophysical granular flows. In this study, we calculate and report the values of all the three angles of internal friction for completeness.

The bed friction angle, φ_{bed} is defined as the angle at which a plane needs to be inclined for the granular material to flow at constant speed (Figure 2). In the basal region, the bed friction angle is equivalent to the wall friction angle. One of the methods of experimentally measuring the wall friction angle is a shear test performed in a shear cell (Figure 2b), where the granular material is compressed at a pre-selected normal stress σ and sheared at a constant rotation rate while the shear stress, τ is measured. The wall friction angle is measured between the granular material and the top part of the shear cell, i.e., the part in contact with the material (here, sandpaper of different grits/roughnesses).

A standard, internationally accepted shear test procedure also exists to determine the wall friction angle, φ_{wall} (Schulze, 2014; ASTM International, 2015). The granular material is consolidated at a given pre-shear normal stress, σ_p (also known as a consolidating stress). Following this, the shearing test is initiated which measures the steady-state shear stress, τ, as a response to the pre-selected normal stress, σ. It is usual to measure the wall friction angle at incrementally decreasing normal stresses (Figure 1c), therefore, the measurements start with the greatest normal stress, σ. The material is sheared at a constant rotation rate while maintaining σ until a constant value of shear stress, τ is achieved (steady-state point). The normal stress, σ is then reduced and the material is sheared until a lower steady-state shear stress is achieved. This routine is typically performed for pre-selected values of σ which are between 20% and 80% of σ_p. Having collected these shear test data, the wall friction angle, φ_{wall} is calculated as the slope of the line going through all the data points on a σ-τ diagram 2c).

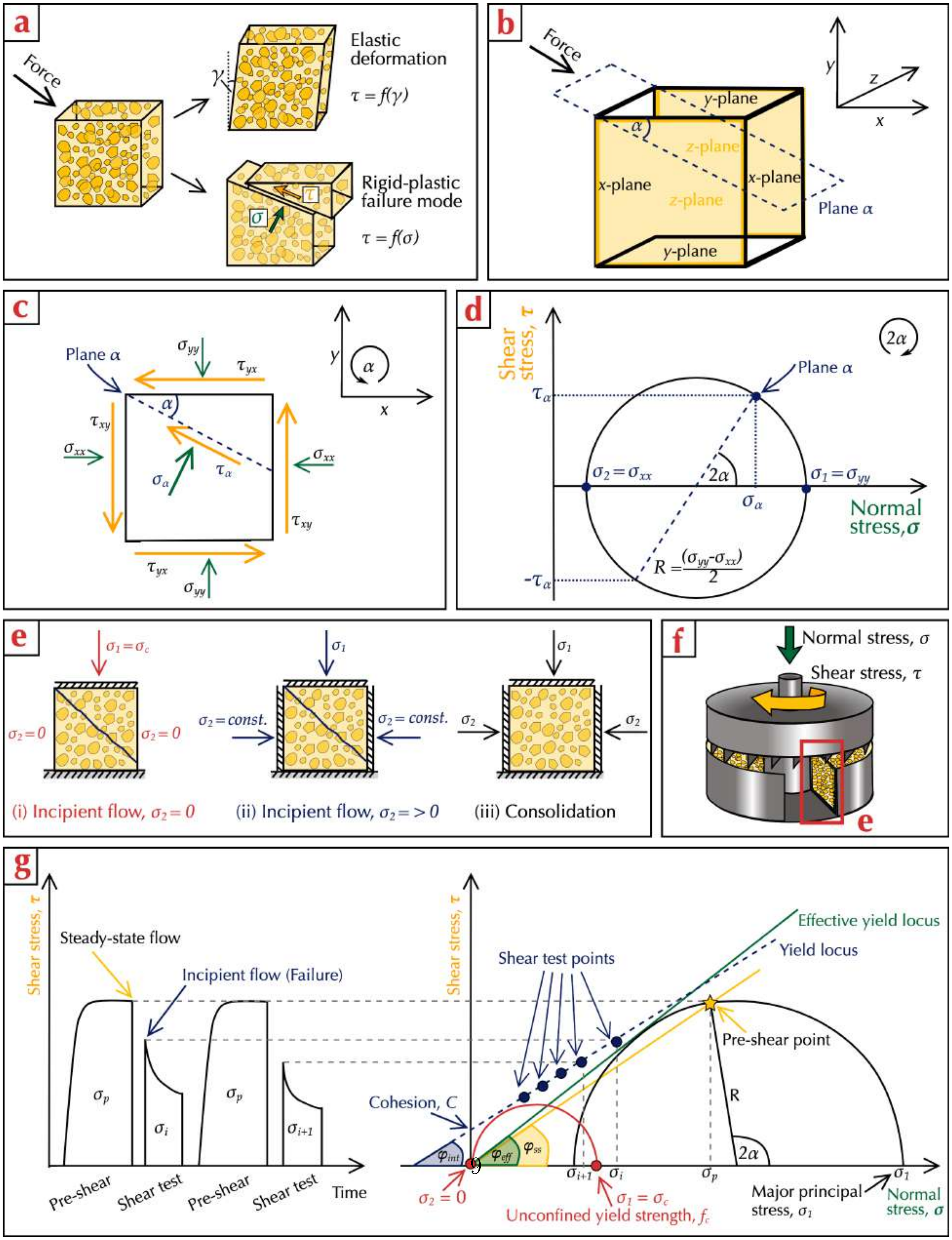

Figure 1: Figure caption on the next page.

Figure 1: A set of diagrams presenting stresses and internal angle measurement methods in bulk solids (granular materials). (a) Response of an element due to the application of a force - elastic deformation (fluids) and rigid-plastic failure mode (bulk solid), where γ is the shear strain, τ is the shear stress and σ is the normal stress. (b) An element of a bulk solid in three dimensions showing the x-, y-, z-plane, and the slip plane α; (c) Stress equilibrium on an element of a bulk solid in two dimensions, in the x-y plane; (d) The Mohr's stress circle in a σ-τ diagram, where σ_1 and σ_2 are the major and minor principal stresses, respectively, R is the radius of the Mohr's circle and α is the inclination angle of the slip plane; (e) Measurement of the unconfined (i) yield strength, (ii) yield locus, and (iii) major principal stress; (f) Schematic of a shear cell apparatus used for our internal angle measurements; (g) Shear test procedure for measuring internal friction angles. Shear stress, τ as a function of time and the corresponding shear test points in a σ-τ diagram, where σ_p is the pre-shear (consolidating) stress, σ_i is the normal stress during the shear test, φ_{int}, φ_{eff}, and φ_{ss} are the angle of internal friction, the effective angle of internal friction, and the steady-state flow angle of internal friction, respectively.

3. Methodology

3.1. Pyroclastic material

All the experiments were performed using pyroclastic material from Bend and Tumalo area in central Oregon, USA (Figure 3a). Bend pumice is a fallout deposit and the overlying deposit sequence H, and Tumalo Tuff are pyroclastic flow deposits, all resulting from a single eruption from a vent west of Bend (Deligne et al., 2017). The deposit was sampled at four locations, A through D. An example of stratigraphic log and a photo of the outcrop, representative of all the four locations sampled, is shown in Figure 3b-c. The deposit consists of a Bend Pumice unit (BP), a sequence H, and a Tumalo Tuff unit (TT). Each unit was divided into respective depositional layers. Here, we focus on measuring friction properties of a pyroclastic flow, and due to the amount of available material, we chose to study layer TT1. The grain size distribution for TT1 for all the four sampled locations (Figure S1 in supporting information), shows that there are only very minor differences in the size distribution between the locations. Therefore, for this study, we mixed TT1 material from all the locations in their respective grain sizes and produced two mixes: one with particles of diameters $0\,\mu m < d < 180\,\mu m$, which we refer to as "fine" herein and a second with particles of diameters $d < 710\,\mu m$, which we refer to as "coarse" herein. These mixes were then split using a riffle box to form a set of homogeneous aliquots used for the

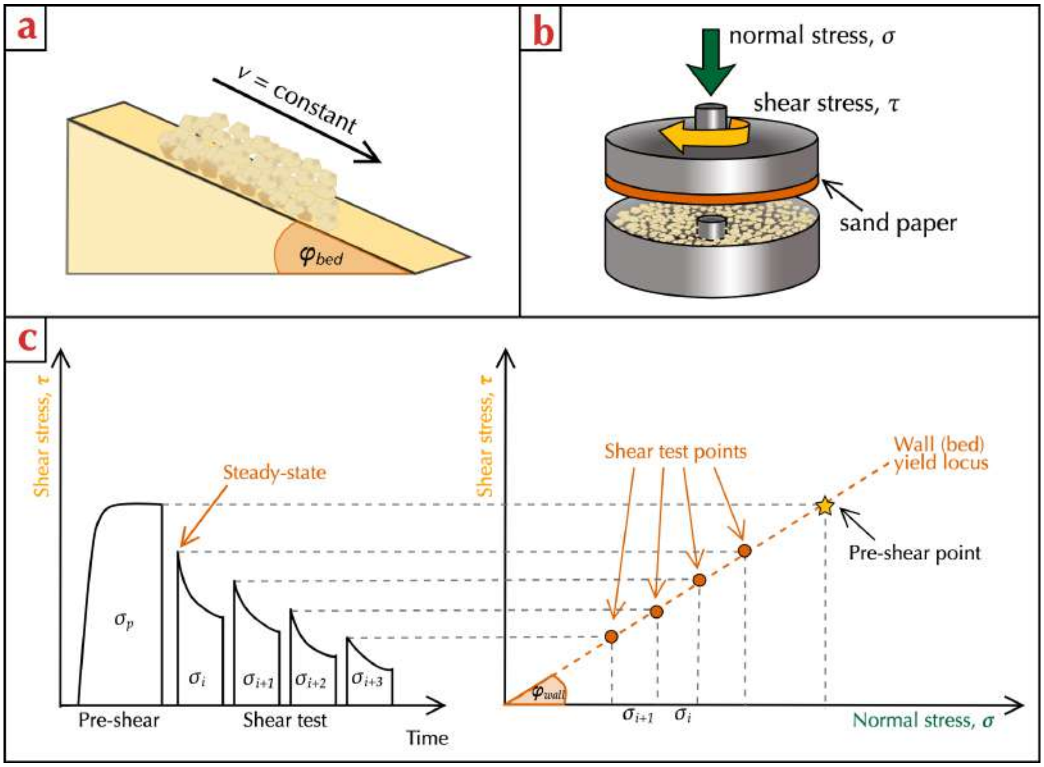

Figure 2: A set of diagrams presenting stresses and wall friction angle measurement methods in bulk solids (granular materials). (a) Illustration of a bed (wall) friction angle, φ_{bed}; (b) Schematic of a shear cell apparatus used for our wall friction angle measurements; (c) Shear test procedure for measuring wall friction angle. Shear stress, τ as a function of time and the corresponding shear test points in a σ-τ diagram, where σ_p is the pre-shear (i.e.,consolidating) stress, σ_i is the normal stress during the shear test, and φ_{wall} is the wall friction angle.

experiments.

The particle size distribution of each mix was measured using a Camsizer X2 particle analyser using a dry dispersion method (with an X-Jet module attached). The Camsizer X2 uses dynamic image analysis, where the particles are dispersed by compressed air and fall vertically through the field of view of two high-resolution cameras, which capture the images of the moving particles. Here, the dispersion pressure was set to 120 kPa. The sample mass analysed by the Camsizer X2 was 3 g and 5 g for the fine and coarse material, respectively. Each measurement was repeated three times. From the images captured by the Camsizer X2, the particle diameter, d, was measured as the minimum width of the particle, and thus is comparable to traditional sieving data. These size distribution data were used to calculate a mean diameter, d_{50}, which informs that 50% of the sample volume is finer than this value. The mean diameter was calculated assuming a linear interpolation between the size fractions. The particle size distribution is presented in Figure 4 and the full dataset is provided in the Supporting Information. The mean diameter, d_{50} is $25 \pm 1\,\mu\mathrm{m}$ and $170 \pm 13\,\mu\mathrm{m}$ for the fine and coarse material, respectively.

The density of the particles that comprise the two mixes was calculated using Anton Paar Ultrapyc 5000 and 5000 Micro helium gas pycnometers. A pycnometer applies the ideal gas law to calculate the volume of the sample of known mass (Webb et al., 1997). The measurement procedure was as follows. A sample of mass m_p was weighed out using Ohaus Pioneer PX224 balance (with readability of 0.1 mg) and loaded into the sample chamber, which was maintained at a constant temperature of 20℃ . The sample chamber was pressurised to the target pressure of 0.69 bar and 1.31 bar for the fine and coarse material, respectively. Then, a valve connecting the sample chamber to a reference chamber was opened, allowing gas to fill the reference chamber. The pycnometer measures the pressure in the sample chamber and the reference chamber and calculates the skeletal volume as

$$V_p = V_{ch} - \frac{V_r}{\frac{p_i}{p_f} - 1}, \tag{10}$$

where V_{ch} is the volume of the empty sample chamber, V_r is the volume of the reference chamber, and p_i and p_f are the initial and final pressures in the sample chamber, respectively. For both the fine and coarse sample sets, in order to obtain a representative value of the volume of the sample, ten measurements were performed for three sample aliquots of different mass. Having the mass and the skeletal volume of the sample, the skeletal particle density was calculated as the gradient of the linear regression to the data. The raw data is provided in the supporting information. The skeletal particle density is $\rho_p = 2391 \pm 2\,\mathrm{kg\ m^{-3}}$ and $2268 \pm 1\,\mathrm{kg\ m^{-3}}$ for the fine and coarse material, respectively.

Before all measurements, the pyroclastic material was dried for 24 hours at 100°C in a laboratory oven to remove any moisture. The material was then kept in a sealed Nalgene$^{\mathrm{TM}}$ desiccator cabinet which protected the samples from any atmospheric water absorption.

3.2. Experimental apparatus

The friction angle experiments were conducted using an Anton Paar MCR302 rheometer with a Powder Shear Cell attached (Figure 5). The Powder Shear Cell consists of a lower measuring cup for the granular material and an upper measuring geometry. The maximum volume of the material in the lower measuring cup is 18.9 mL. For the measurements of the angle of internal friction, the measuring geometry is 32 mm in diameter with 12 evenly spaced fins, which are 2 mm in length (Figure 5). For the measurements of the wall friction angle, the measuring geometry is 32 mm in diameter and has a removable plate to measure the friction between the granular material and the plate. The measuring geometry rotates at n rotations per minute, shearing the granular material and applying torque, M, defined as

$$M = \frac{\tau}{CSS}, \tag{11}$$

where τ is the shear stress and CSS is a Controlled Shear Stress (CSS) geometry factor, typically determined by calibration against a Newtonian material of known viscosity (Whorlow, 1992; Mezger, 2012; Mader et al., 2013). Here, the measuring geometry is based on ISO standard 3219 and has a CSS geometry factor of $162492.82\,\mathrm{m}^{-3}$ and $12355.2\,\mathrm{m}^{-3}$ for the measurements of the internal friction angle and wall friction angle, respectively.

In order to investigate the wall friction angle for surfaces or flow substrates of different roughness, we attached disks laser cut out of sandpaper sheets of different grit number to the base of the measuring geometry. The sandpaper grit number, no_g corresponds to sand particles of diameter d_s, and thus roughness, calculated using

$$d_s = 11764.71 \times no_g^{-0.93589}. \tag{12}$$

ANSI (2018) requires that the commercially available abrasive materials satisfy this relationship within a 3% accuracy. Therefore, the sandpaper used in this study of grit 40, 60, 120, 240, 320, and 400 corresponds to sand particles of diameters $370 \pm 10\,\mu\mathrm{m}$, $255 \pm 8\,\mu\mathrm{m}$, $133 \pm 4\,\mu\mathrm{m}$, $70 \pm 2\,\mu\mathrm{m}$, $53 \pm 2\,\mu\mathrm{m}$, and 43 ± 1 µm, respectively (Figure 6).

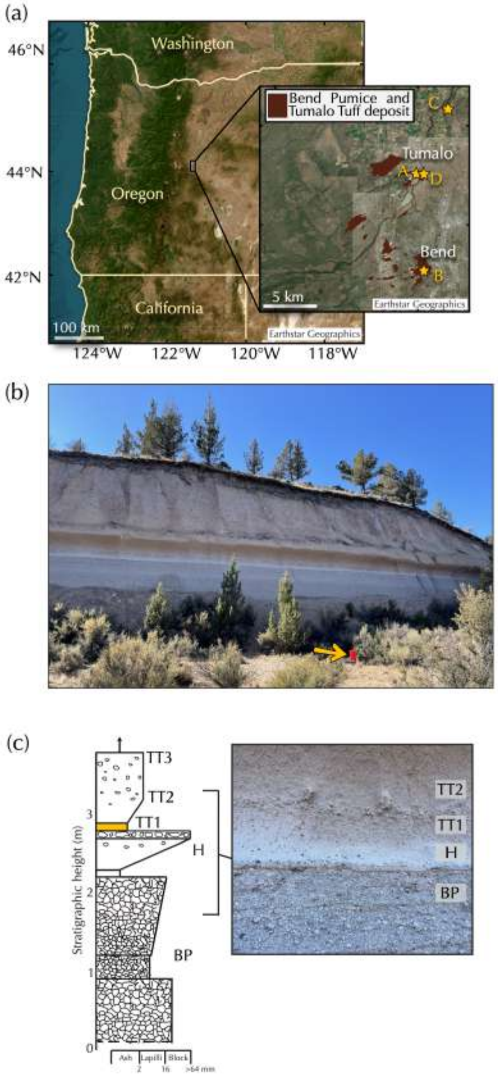

Figure 3: Location and properties of the pyroclastic material used in this study. (a) Map of the central west coast of the US, showing the state of Oregon and the city of Bend. Basemap from The MathWorks Inc. (2022) and created using Esri, HERE, Garmin, NGA, USGS, NPS. The zoomed-in map shows Bend and Tumalo area. The yellow stars represent the sampled locations A through D. Tumalo Tuff and Bend Pumice deposits locations from Deligne et al. (2017). Basemap from The MathWorks Inc. (2022) created using Bureau of Land Management, State of Oregon GEO, Esri, HERE, Garmin, INCREMENT P, NGA, USGS, U.S. Forest Service. (b) Outcrop photograph of location A taken by authors. The red arrow points to a bucket of height of approximately 37 cm. (c) Example stratigraphic log of one of the sampled locations (Location A, Tumalo Reservoir Road, 44.13394 N, 121.33814 W). BP, H, and TT stand for Bend Pumice, Deposit Sequence H, and Tumalo Tuff, respectively.

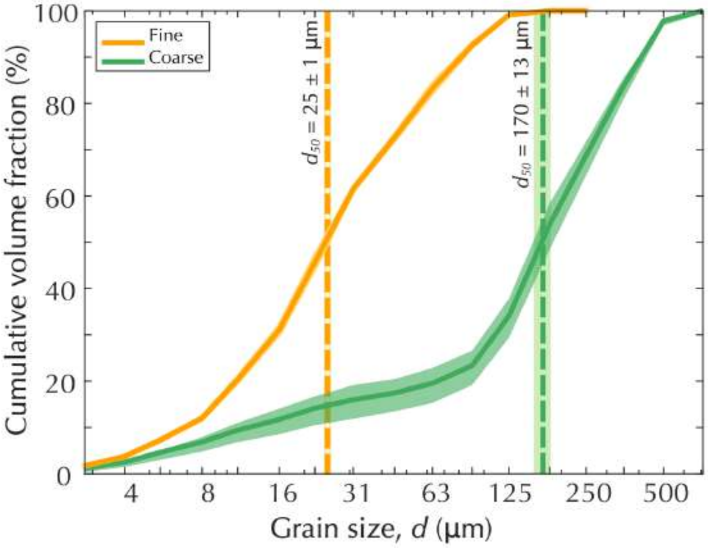

Figure 4: Particle size distribution for the fine and coarse material used for the experiments in this study. The dashed lines correspond to the mean diameter d_{50}. The shaded areas represent the 95% confidence intervals.

3.3. Experimental procedure

3.3.1. Internal friction angle

The experimental procedure for measuring the internal friction angle includes sample preparation and shear measurements and follows guidance from ASTM International (2015). The material is weighed out and loaded into the measuring cup. The measuring geometry is then lowered down such that it is in contact with the sample and the material is consolidated at the target pre-shear normal stress, σ_p (also known as consolidating stress) for 60 seconds. Then, the material is sheared at $n = 0.005$ rotations per minute while maintaining σ_p until a steady state torque, M, has been achieved (within 0.2% tolerance error). The same pre-shearing cycle is performed by rotating the measuring geometry in the opposite direction. This completes the initial pre-shearing (consolidating) requirements. Additionally, using the input mass of the granular material, the vertical position of the measuring geometry, and the initial volume of the sample (i.e., the maximum volume of the shear cell, $V = 18.9\,\mathrm{mL}$), the rheometer calculates its bulk density, ρ, i.e., the density of the material in the shear cell consolidated (i.e., reduced in volume) at a specific value of σ_p. Following this, the shearing test is

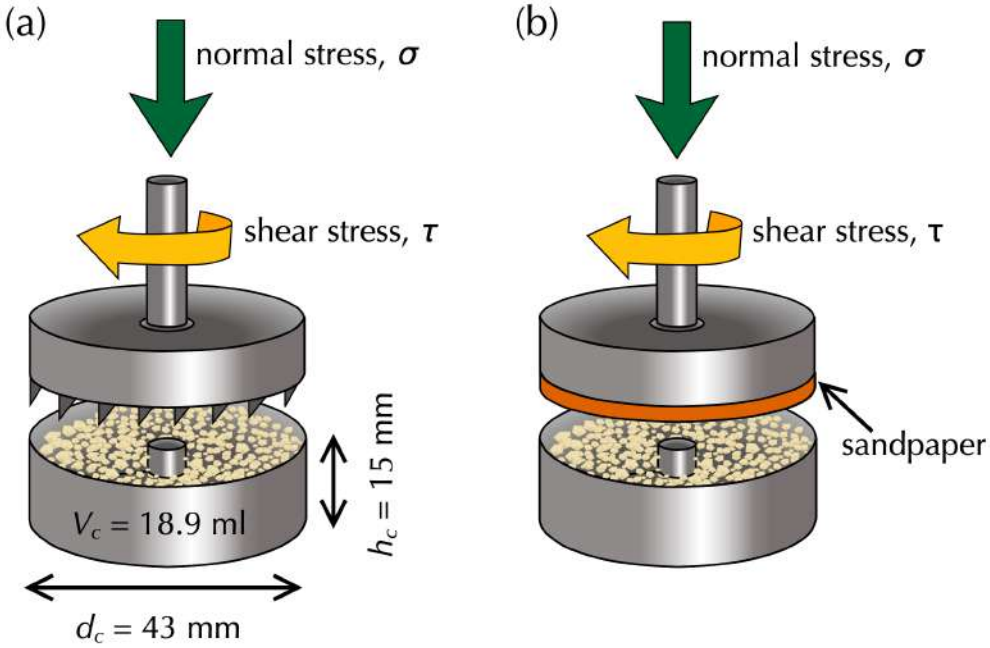

Figure 5: Diagram of the experimental apparatus. (a) The shear cell with the measuring geometry for the measurements of the angle of internal friction. (b) The shear cell with the measuring geometry and sandpaper for the measurement of the angle of wall friction. The same shear cell (the bottom part of the apparatus) is used for both measurements, where V_c, h_c, and d_c are the volume, the height, and the diameter of the cell, respectively.

initiated which measures the maximum shear stress, τ, as a response to the pre-selected normal stress, σ at a prescribed pre-shear normal stress, σ_p. The shearing test begins with a single pre-shearing cycle at $n = 0.005$ rotations per minute at σ_p. Secondly, the normal stress is lowered to σ and the material is consolidated at σ for 40 seconds at $n = 0$ rotations per minute. Finally, the material is sheared at $n = 0.005$ rotations per minute while maintaining σ until a maximum shear stress, τ is achieved and τ has subsequently reduced. This routine is performed for all the measuring points, i.e., all the pre-selected values of σ. In our experiments, the pre-selected values of normal stress, σ were chosen to be 20, 35, 50, 65, and 80% of σ_p (Table 1). In order to enhance repeatability of the measurements and ensure consistency of the granular material, each sample was used only once and a new sample

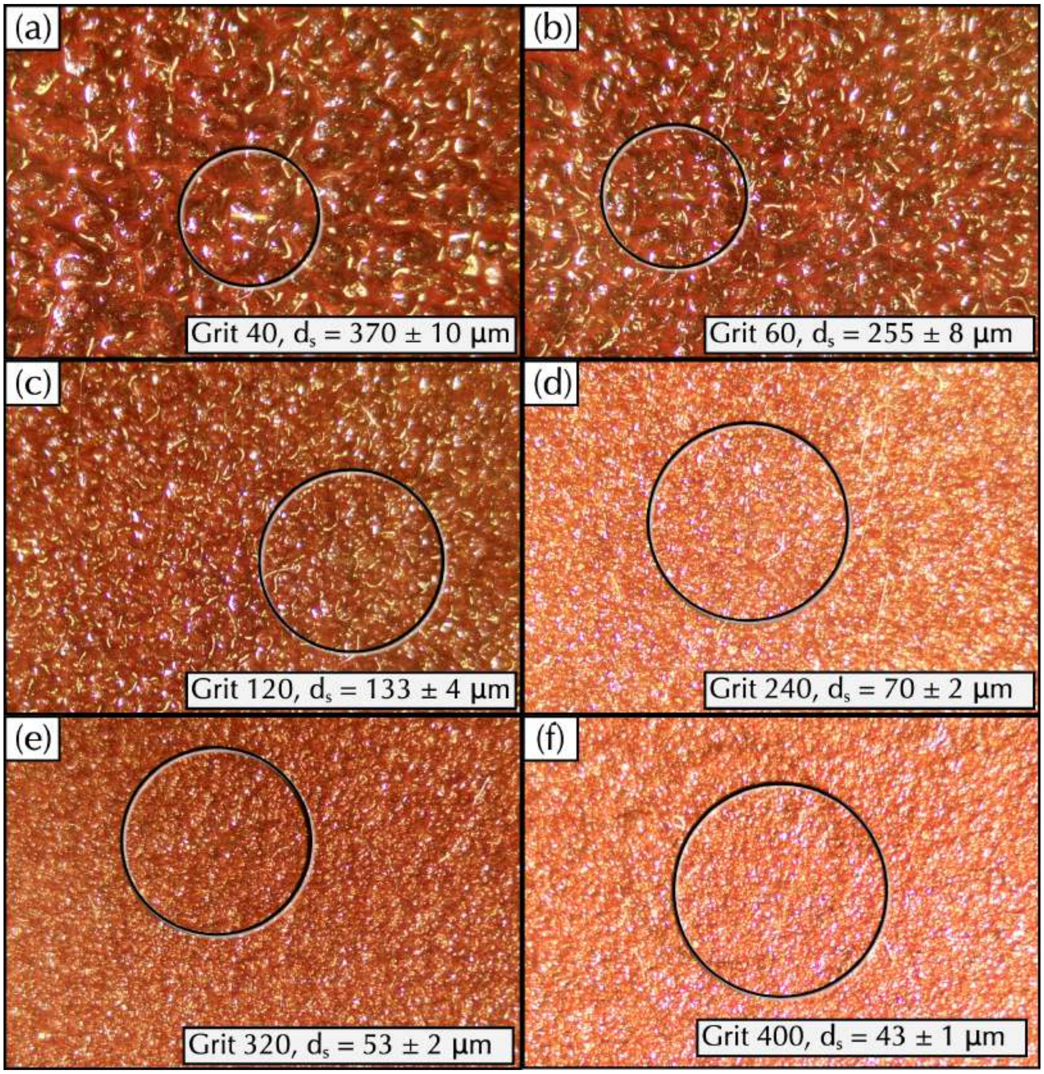

Figure 6: Binocular microscope images of the sandpaper of grit (a) 40, (b) 60, (c) 120, (d) 240, (e) 320, and (f) 400 taken under a binocular microscope. The black circles are used as a common reference scale and are of diameter 4 mm in all images.

was loaded into the shear cell before each measurement. The grain size distribution before and after the measurements is provided in the Supporting Information. Due to the amount of available material, the experiments using fine material were performed at pre-shear normal stress of $\sigma_p = 1.5$, 3.0, 4.5, 6.0, 7.5, and 9.0 kPa, where σ_p = 3.0, 6.0, and 9.0 kPa were repeated five times, and σ_p = 1.5, 4.5, and 7.5 kPa were performed once. The experiments using coarse material were performed at pre-shear normal stress of σ_p = 3.0, 6.0, and 9.0 kPa, where all the experiments were repeated three times. The number of repeats performed for each measurement condition is provided in Table 1.

3.3.2. Wall friction angle

Similarly to the measurements of the internal friction angle, the experimental procedure for measuring the wall friction includes both sample preparation and shear measurements ASTM International (2015). The material is weighed out and loaded into the measuring cup. A sandpaper disk is attached to the plate with adhesive tape, which is then attached to the measuring geometry. Each sandpaper disk was used only once and a new disk was attached to the plate before each measurement. The measuring geometry is lowered down such that it is in contact with the sample and the material is consolidated at the target pre-shear normal stress, σ_p for 50 seconds. Then, the material is sheared at $n = 0.05$ rotations per minute while maintaining σ_p. This completes the initial pre-shearing (consolidating) requirements. As for the internal friction measurements, the rheometer calculates the bulk density of the granular material, ρ consolidated at a specific value of σ_p. Following this, the shearing test is initiated which measures the steady-state shear stress, τ, as a response to the pre-selected normal stress, σ at a prescribed pre-shear normal stress, σ_p. The shearing test begins with lowering the normal stress to σ and consolidating the material at σ for 50 seconds at $n = 0$ rotations per minute. Secondly, the material is sheared at $n = 0.005$ rotations per minute while maintaining σ until a steady-state shear stress, τ is achieved. This routine is performed for all the measuring points, i.e., all the pre-selected values of σ. In our experiments, the pre-selected values of normal stress, σ were chosen to be 20, 40, 60, and 80% of σ_p (Table 2). Due to the amount of available material, the experiments using fine material were performed at pre-shear normal stress of σ_p = 3.0, 6.0, and 9.0 kPa using sandpaper of d_s = 370 ± 10 µm, 255 ± 8 µm, 133 ± 4 µm, 70 ± 2 µm, 53 ± 2 µm, and 43 ± 1 µm, which corresponds to the roughness ratio d_{50}/d_s = 0.07 ± 0, 0.10 ± 0, 0.19 ± 0.01, 0.35 ± 0.01, 0.46 ± 0.02, and 0.57 ± 0.02. The experiments using coarse material were performed at pre-shear normal stress of σ_p = 3.0, 6.0, and 9.0 kPa using sandpaper of using sandpaper of d_s = 370 ± 10 µm, 133 ± 4 µm, and 53 ± 2 µm, which corresponds to the roughness

Table 1: Normal stress, σ and number of repeats, *no* for each pre-shearing normal stress, σ_p for internal friction angle measurements.

σ_p (kPa)	σ (kPa)					*no* FINE	*no* COARSE
9.0	1.80	3.15	4.50	5.85	7.20	5	3
7.5	1.50	2.63	3.75	4.88	6.00	1	-
6.0	1.20	2.10	3.00	3.90	4.80	5	3
4.5	0.90	1.58	2.25	2.93	3.60	1	-
3.0	0.60	1.05	1.50	1.95	2.40	5	3
1.5	0.30	0.53	0.75	0.98	1.20	1	-

ratio $d_{50}/d_s = 0.46 \pm 0.04$, 1.27 ± 0.14, and 3.19 ± 0.71. The number of repeats performed for each measurement condition is provided in Table 2.

4. Results and analysis

4.1. Internal friction angle

Figure 7a presents an example of the raw data collected by the rheometer, i.e., the shear stress, τ and the normal stress, σ data as a function of time. The figure also indicates the pre-shearing (consolidating) interval (stars) and the shear test intervals (circles). As explained in Section 3, for the calculations of the internal friction angles, the pre-shear data point is the pre-selected value of the normal stress and the maximum value of the measured shear stress. The shear test data points are the maximum values of the normal and the shear stress in the shear test interval. The data presented in Figure 7 are representative of all the performed measurements and all the data were processed and analysed using the methods described in the previous section. A full raw dataset is provided in the online repository as referenced in the Open Research Section.

The measurements of the bulk density, ρ, the internal friction angle, φ_{int}, the effective internal friction angle, φ_{eff}, and the internal friction angle at a steady-state flow, φ_{ss} for fine and coarse material are reported in Table 3. Figure 8 presents the shear test data for the measurements of the internal friction angles. Since the internal friction is a result of particles moving against each other, it must depend on the physical properties of particles, such as size, shape, angularity, and surface texture (e.g., Cagnoli and Manga,

Table 2: Normal stress, σ and number of repeats, *no* for each pre-shearing normal stress, σ_p and roughness ratio, d_{50}/d_s for wall friction angle measurements.

	σ_p (kPa)	σ (kPa)				d_{50}/d_s	no
FINE	9.0	1.8	3.6	5.4	7.2	0.07 ± 0.00	3
						0.10 ± 0.00	1
						0.19 ± 0.01	3
						0.35 ± 0.01	1
						0.46 ± 0.02	3
						0.57 ± 0.02	1
FINE	6.0	1.2	2.4	3.6	4.8	0.07 ± 0.00	3
						0.10 ± 0.00	1
						0.19 ± 0.01	3
						0.35 ± 0.01	1
						0.46 ± 0.02	3
						0.57 ± 0.02	1
FINE	3.0	0.6	1.2	1.8	2.4	0.07 ± 0.00	3
						0.10 ± 0.00	1
						0.19 ± 0.01	3
						0.35 ± 0.01	1
						0.46 ± 0.02	3
						0.57 ± 0.02	1
COARSE	9.0	1.8	3.6	5.4	7.2	0.46 ± 0.04	3
						1.27 ± 0.14	3
						3.19 ± 0.71	3
COARSE	6.0	1.2	2.4	3.6	4.8	0.46 ± 0.04	3
						1.27 ± 0.14	3
						3.19 ± 0.71	3
COARSE	3.0	0.6	1.2	1.8	2.4	0.46 ± 0.04	3
						1.27 ± 0.14	3
						3.19 ± 0.71	3

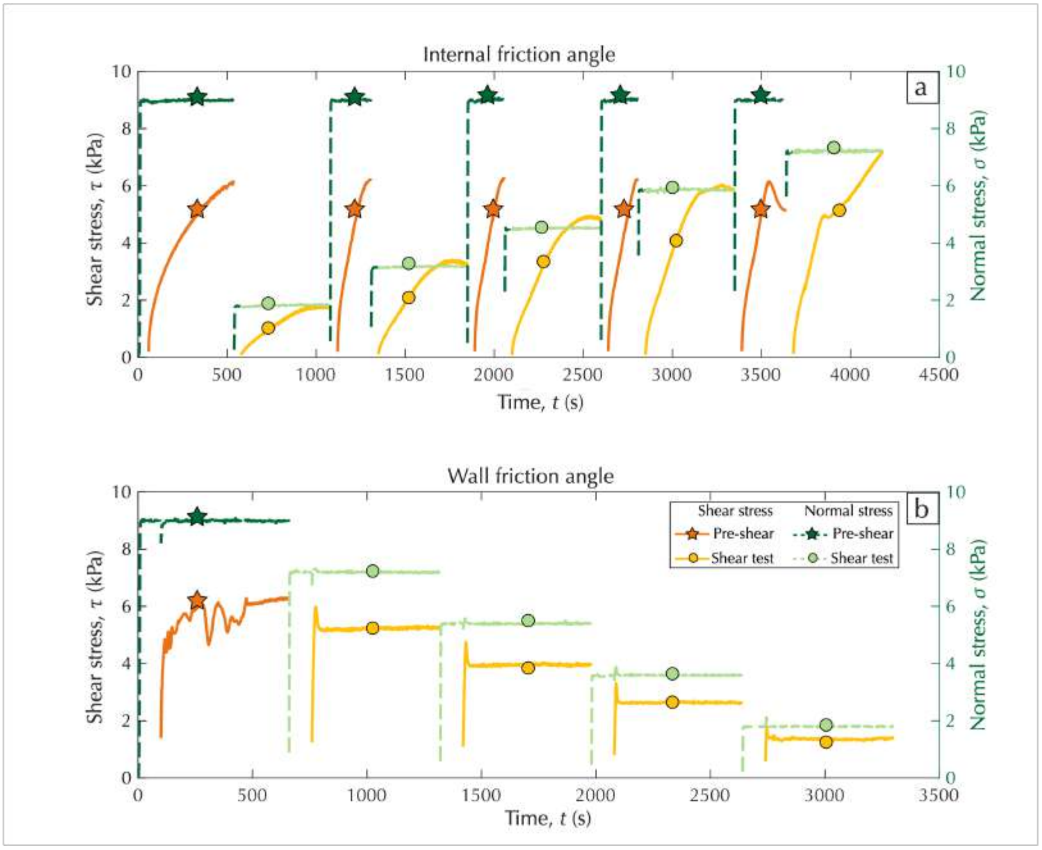

Figure 7: Example of the raw data collected by the rheometer for (a) Measurements of the internal friction angles and (b) Measurements of the wall friction angle. The solid lines and the left-hand-side y-axis correspond to the measurements of the shear stress, τ, while the dashed lines and the right-hand-side y-axis correspond to the normal stress, σ. The stars indicate the pre-shear (consolidating) intervals and the circles indicate the shear test intervals. These symbols are used only to differentiate between the intervals and do not correspond to any real data points.

2004; Samuelson et al., 2008; Vangla and Latha, 2015). Here, we analyse the impacts of particle size, and related to this, the bulk density of the material. The mean diameter for the fine material is nearly seven times smaller than the mean diameter for the coarse material, and the average bulk density pre-consolidation, i.e., $\sigma_p = 0\,\mathrm{kPa}$, is $\rho_0 = 820 \pm 21\,\mathrm{kg\ m^{-3}}$ and $\rho_0 = 670 \pm 18\,\mathrm{kg\ m^{-3}}$ for the fine and the coarse material, respectively. Figure 9 shows that as the material is consolidated with greater pre-shear normal stress, σ_p, the bulk density, ρ increases. This change is much more pronounced for the fine material which supports previous studies (Shi et al., 2018; Samuelson et al., 2008). The average bulk density for the consolidated material is $\rho = 1018 \pm 41\,\mathrm{kg\,m^{-3}}$ and $\rho = 707 \pm 21\,\mathrm{kg\,m^{-3}}$ for the fine and the coarse material, respectively, which gives the normalised bulk density ρ/ρ_0 between 1.09 and 1.36 for the fine material and between 1.04 and 1.06 for the coarse material.

Although the fine material consolidated at $\sigma_p = 9\,\mathrm{kPa}$ generates a granular mixture that is more dense than at $\sigma_p = 1.5\,\mathrm{kPa}$, this difference appears to be insignificant as there is no clear relationship between σ_p and any of the internal friction angles. Similarly, for the coarse material, there are only minor fluctuations in the internal friction angles with σ_p. However, all the internal friction angles are smaller for the fine material compared to the coarse material (Figure 9a). For the fine material, the internal friction angle falls in the range $\varphi_{int} = 44.9°$ - $48.8°$, the effective internal friction angle is in the range $\varphi_{eff} = 45.3°$ - $48.5°$, and the steady state internal friction angle is in the range $\varphi_{ss} = 34.1°$ - $42.4°$. For the coarse material, the internal friction angle falls in the range $\varphi_{int} = 48.2°$ - $53.6°$, the effective internal friction angle is in the range $\varphi_{eff} = 49.4°$ - $53.9°$, and the steady state internal friction angle is in the range $\varphi_{ss} = 40.6°$ - $49.5°$. Cohesion, C of the granular material was determined as the intercept of the yield locus with the τ-axis, where the yield locus is a linear regression fitted to the shear data. Interestingly, only measurements at $\sigma_p = 9\,\mathrm{kPa}$ (our highest consolidation/pre-shear stress used) have non-zero cohesion, however, this is not universally true and only reported for some of the repeats, giving average cohesion values with large relative errors, $C = 0.08 \pm 0.09\,\mathrm{kPa}$ and $0.34 \pm 0.30\,\mathrm{kPa}$ for the fine and coarse material, respectively. The average coefficient of determination, R^2 is 0.99 ± 0.01 and 0.97 ± 0.01, for the fine and coarse material, respectively. The average Root Mean Square Error, $RMSE$ is 0.12 ± 0.09 and 0.38 ± 0.20. The values of C, R^2, and $RMSE$ for all the test repeats are provided in the Supporting Information.

Higher internal friction angles suggest that the coarse material can withstand greater stress before failing (flowing). If we were to imagine a sufficiently great external force acting on a bulk solid that one particle's energy increases and it moves, this particle will then transfer the energy to a neighbouring particle. The amount of the transferred energy depends on how much of the energy is lost in the gap between the two particles. In general, the larger the particles, the larger the inter-particle gaps and the more energy is lost. On the other hand, the smaller inter-particle gaps in the fine material mean that the particles stay in contact with each other for a longer duration, minimising energy losses. Therefore, in general, bulk solids composed of finer material are more susceptible to failure, which means they are more flowable.

4.2. Wall friction angle

Figure 7b presents an example of the raw data collected by the rheometer, i.e., the shear stress, τ and the normal stress, σ data as a function of time. These data are representative of all measurements performed and all these data were processed and analysed using the methods described within Section 3.

The wall friction angle was measured between the pyroclastic material and the sandpaper with the roughness ratio d_{50}/d_s = 0.07-3.90. The shear test data is presented in Figure 10 and in Table 4. While the bulk density does not affect the wall friction angles in the same way as it does the internal friction, we report the bulk density values for completeness. For the fine material, for d_{50}/d_s = 0.07 ± 0, the wall friction angle is in the range φ_{wall} = 31.7° - 39.0°, for d_{50}/d_s = 0.10 ± 0, φ_{wall} = 33.7° - 36.3°, for d_{50}/d_s = 0.19 ± 0.01, φ_{wall} = 31.9° - 37.5°, for d_{50}/d_s = 0.35 ± 0.01, φ_{wall} = 35.5° - 36.1°, for d_{50}/d_s = 0.46 ± 0.02, φ_{wall} = 32.2° - 36.7°, and for d_{50}/d_s = 0.57 ± 0.02, φ_{wall} = 33.9° - 35.8°. For the coarse material, for d_{50}/d_s = 0.46 ± 0.04, the wall friction angle is in the range φ_{wall} = 32.3° - 40.5°, for 1.27 ± 0.14, φ_{wall} = 29.5° - 37.4°, and for d_{50}/d_s = 3.19 ± 0.71, φ_{wall} = 27.4° - 36.8°.

The wall friction angle appears to be slightly lower for a larger d_{50}/d_s ratio, however, there is no clear relationship between the measurements and the roughness ratio. Therefore, we performed a statistical analysis which considered all the measurements (including repeats) for a given d_{50}/d_s ratio. In order to keep the data consistent, only the measurements with three repeats were included in the analysis. This gives six roughness ratio groups d_{50}/d_s = 0.07 ± 0, 0.19 ± 0.01, 0.46 ± 0.02, 0.46 ± 0.04, 1.27 ± 0.14, and 3.19 ± 0.71 with nine measurements in each group. The repeated d_{50}/d_s = 0.46 corresponds to the measurements using fine and coarse material. We used a one-way analysis of variance (ANOVA) which is a technique to determine whether data from several groups have a common mean (e.g., Doncaster and Davey, 2007). The analysis was performed in Matlab2022b using anova1

Table 3: Measurements of the bulk density, ρ, the normalised bulk density, ρ/ρ_0, where ρ_0 is the average bulk density pre-consolidation, the internal friction angle, φ_{int}, the effective internal friction angle, φ_{eff}, and the steady state internal friction angle, φ_{ss} for fine and coarse material for pre-shearing stress σ_p. Zero error corresponds to the measurements that were performed only once.

	σ_p (kPa)	ρ (kg m^{-3})	ρ/ρ_0	φ_{int} (°)	φ_{eff} (°)	φ_{ss} (°)
FINE	9.0	1060 ± 10	1.32 ± 0.04	45.4 ± 0.6	45.9 ± 0.6	38.4 ± 4.3
	7.5	1050 ± 0	1.29 ± 0.00	48.0 ± 0.0	48.0 ± 0.0	42.4 ± 0.0
	6.0	1040 ± 10	1.25 ± 0.09	47.5 ± 0.8	47.5 ± 0.8	42.9 ± 1.3
	4.5	1010 ± 0	1.20 ± 0.00	48.5 ± 0.0	48.5 ± 0.0	41.8 ± 0.0
	3.0	1000 ± 0	1.27 ± 0.00	47.8 ± 0.0	47.8 ± 1.0	41.3 ± 0.5
	1.5	950 ± 0	1.15 ± 0.06	45.6 ± 1.0	46.3 ± 0.0	37.6 ± 0.0
COARSE	9.0	730 ± 30	1.05 ± 0.01	50.6 ± 0.7	52.7 ± 1.2	44.4 ± 3.8
	6.0	700 ± 20	1.05 ± 0.00	52.3 ± 1.3	52.3 ± 1.3	48.0 ± 1.6
	3.0	690 ± 10	1.05 ± 0.01	49.8 ± 1.6	51.4 ± 2.0	47.8 ± 0.4

and multcompare functions which computed test statistic, F, and a p-value, where the p-value is a probability that the test statistic can take a value greater than F (The MathWorks Inc., 2022). A p-value smaller than 0.05 is considered as a statistically significant difference. Thus, the ANOVA analysis informs whether there is a statistically significant difference between the roughness ratio groups. The smallest p-value, $p = 0.07$, was calculated between the groups with the smallest and the largest d_{50}/d_s, i.e., $d_{50}/d_s = 0.07$ ± 0 and $d_{50}/d_s = 3.19$ ± 0.71. None of the groups, however, have p-value < 0.05, which means that none of the groups are statistically different from each other. Thus, for our experiments, the wall friction angles did not depend on the roughness ratio. The p-values for all the groups are provided in the Supporting Information.

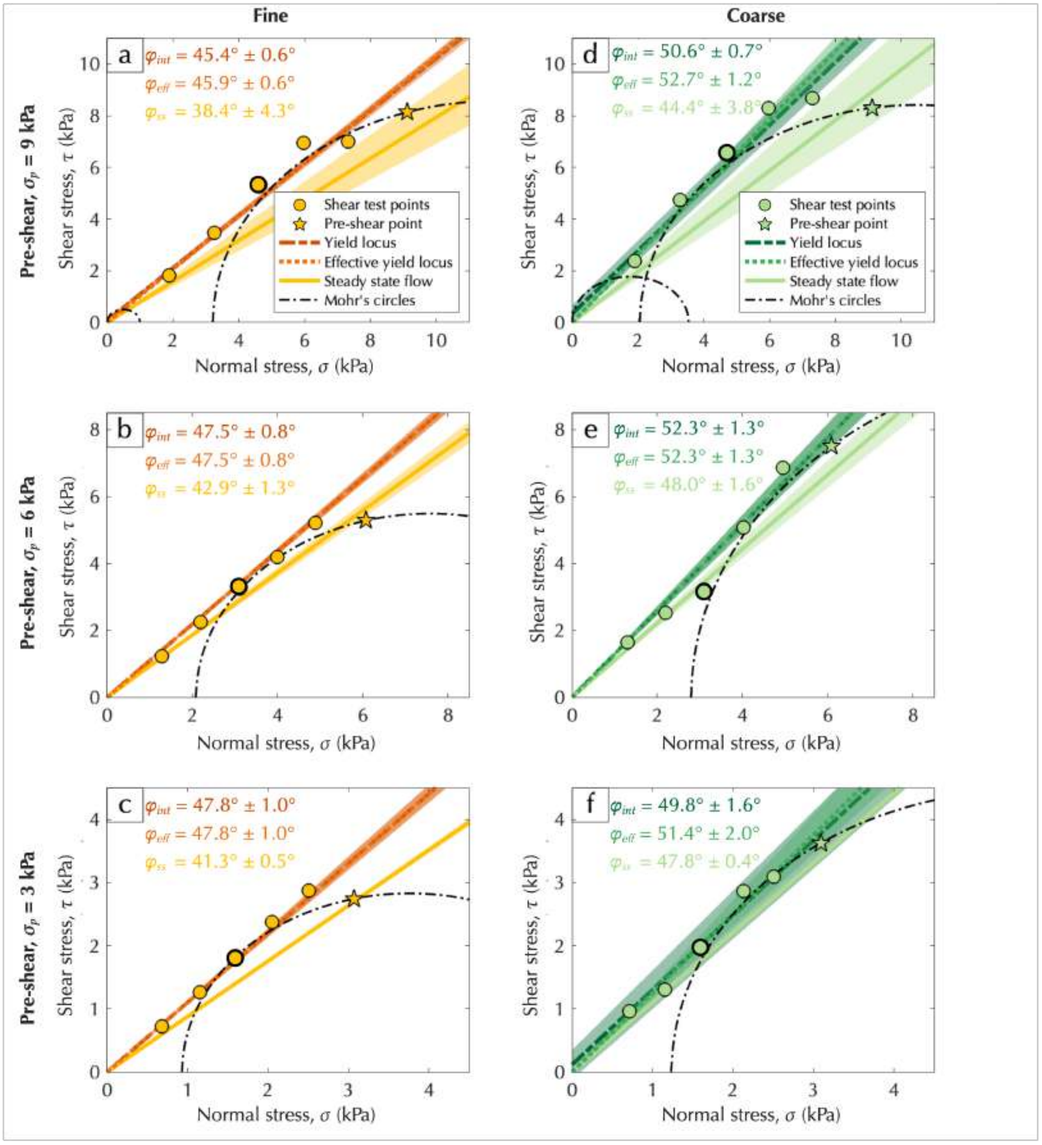

Figure 8: Shear test data (circles) for (a)-(c) fine material, and (d)-(f) coarse material for pre-shear normal stress (stars) $\sigma_p = 9\,\mathrm{kPa}$ (top row), $6\,\mathrm{kPa}$ (middle row), and $3\,\mathrm{kPa}$ (bottom row). The dashed, dotted, and solid lines show the yield locus, the effective yield locus, and the steady state flow yield locus, respectively. The slopes of those lines are the internal friction angle, φ_{int}, the effective internal friction angle, φ_{eff}, and the steady state flow internal friction angle, φ_{ss}. The shaded areas represent the 95% confidence intervals. The black dash-and-dot lines are the Mohr's circles plotted for a given shear test data point (circle with a thick black border) and the pre-shear point (star).

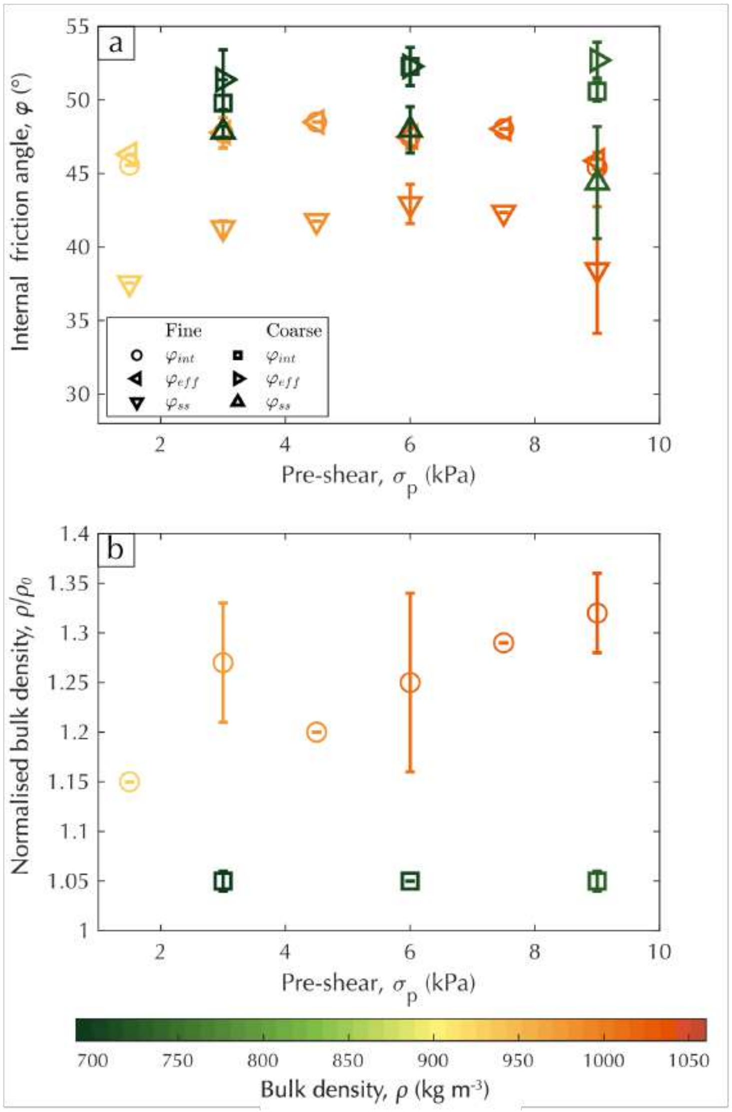

Figure 9: Bulk solid properties as a function of pre-shear normal stress, σ_p. (a) Internal friction angle, φ_{int}, effective internal friction angle, φ_{eff}, and steady state flow internal friction angle, φ_{ss}, (b) Normalised bulk density, ρ/ρ_0 for the internal friction measurements. The symbols are coloured according to the bulk density of the sample, ρ consolidated at normal stress σ_p. The error bars for $\sigma_p = 1.5$, 4.5, and 7.5 kPa are zero because the measurements were performed only once.

Table 4: Measurements of the bulk density, ρ, the normalised bulk density, ρ/ρ_0, where ρ_0 is the average bulk density pre-consolidation, and the wall friction angle, φ_{wall} for fine and coarse material for pre-shearing stress σ_p and roughness ratio, d_{50}/d_s. Zero error corresponds to the measurements that were performed only once.

		9 kPa			6 kPa			3 kPa		
	d_{50}/d_s	ρ (kg m^{-3})	ρ/ρ_0	φ_{wall} (°)	ρ (kg m^{-3})	ρ/ρ_0	φ_{wall} (°)	ρ (kg m^{-3})	ρ/ρ_0	φ_{wall} (°)
FINE	0.07 ± 0.00	1090 ± 0	1.28 ± 0.05	36.0 ± 1.1	1080 ± 10	1.27 ± 0.00	36.5 ± 0.9	1050 ± 10	1.21 ± 0.01	35.4 ± 3.6
	0.10 ± 0.00	1080 ± 0	1.26 ± 0.00	36.3 ± 0.0	1070 ± 0	1.20 ± 0.00	34.7 ± 0.0	1030 ± 0	1.16 ± 0.0	33.7 ± 0.0
	0.19 ± 0.01	1040 ± 0	1.19 ± 0.03	35.4 ± 1.2	1030 ± 0	1.18 ± 0.01	34.4 ± 0.3	1010 ± 10	1.16 ± 0.03	34.7 ± 2.8
	0.35 ± 0.01	1040 ± 0	1.16 ± 0.00	36.1 ± 0.0	1020 ± 0	1.17 ± 0.00	35.5 ± 0.0	1000 ± 0	1.14 ± 0.00	35.6 ± 0.0
	0.46 ± 0.02	1040 ± 20	1.17 ± 0.05	35.6 ± 0.9	1030 ± 10	1.14 ± 0.02	33.4 ± 0.5	1000 ± 20	1.15 ± 0.06	34.4 ± 2.3
	0.57 ± 0.02	1030 ± 0	1.19 ± 0.00	35.8 ± 0.0	1030 ± 0	1.14 ± 0.00	34.4 ± 0.0	1000 ± 0	1.11 ± 0.00	33.9 ± 0.0
COARSE	0.46 ± 0.04	780 ± 10	1.13 ± 0.01	37.8 ± 2.7	780 ± 30	1.12 ± 0.02	34.4 ± 2.1	790 ± 20	1.12± 0.01	34.8 ± 1.3
	1.27 ± 0.14	750 ± 20	1.09 ± 0.00	35.3 ± 2.1	740 ± 30	1.08 ± 0.00	33.9 ± 0.8	720 ± 20	1.08 ± 0.01	30.5 ± 1.0
	3.19 ± 0.71	730 ± 10	1.08 ± 0.00	35.1 ± 1.7	720 ± 10	1.07 ± 0.00	33.8 ± 1.4	720 ± 20	1.07 ± 0.00	30.3 ± 2.8

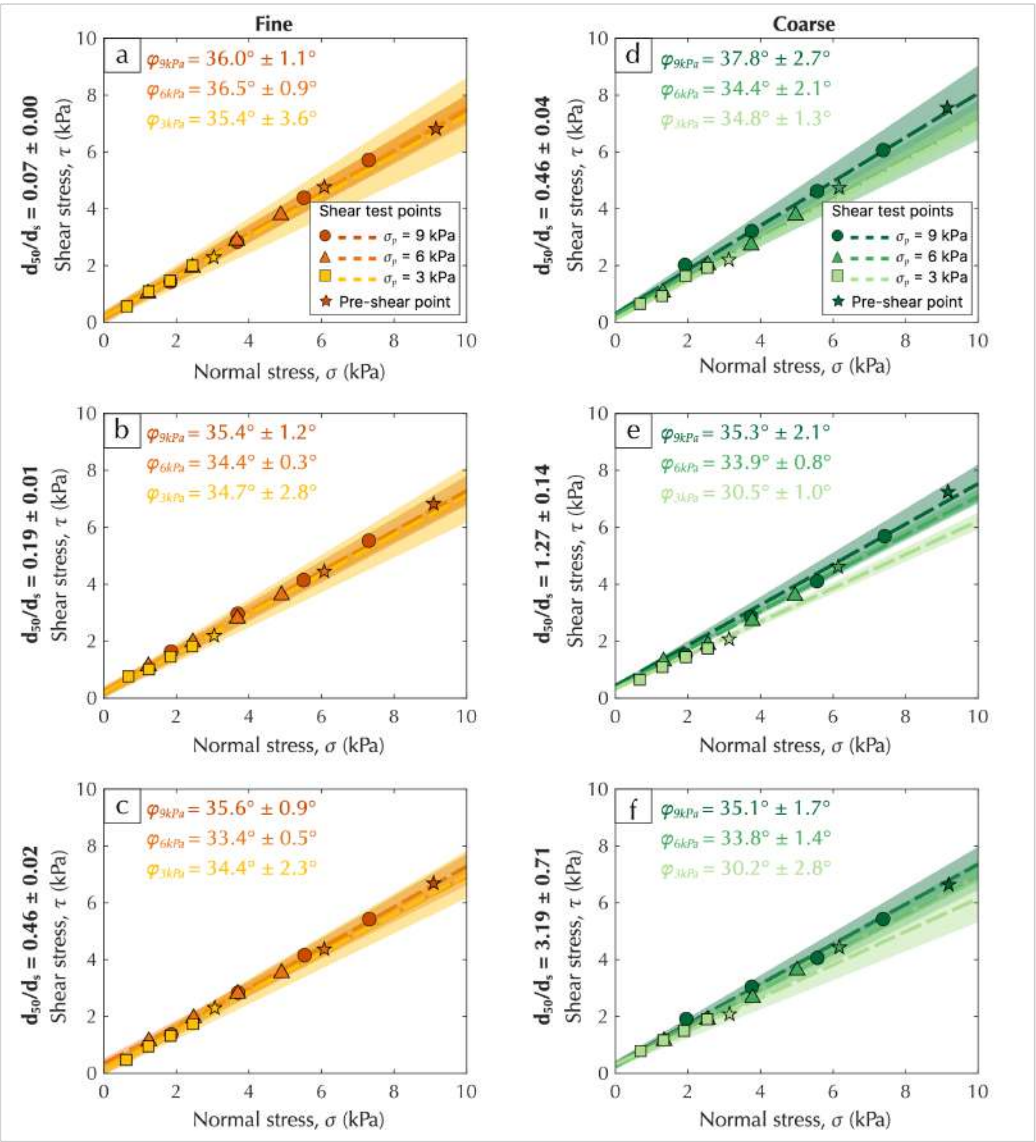

Figure 10: Wall friction shear test data for (a)-(c) fine material, and (d)-(f) coarse material for pre-shear normal stress (stars) $\sigma_p = 9\,\mathrm{kPa}$, $6\,\mathrm{kPa}$, and $3\,\mathrm{kPa}$. The dashed lines show the wall yield locus and the shaded areas represent the 95% confidence intervals. The slope of those lines is the wall friction angle, φ_{wall}.

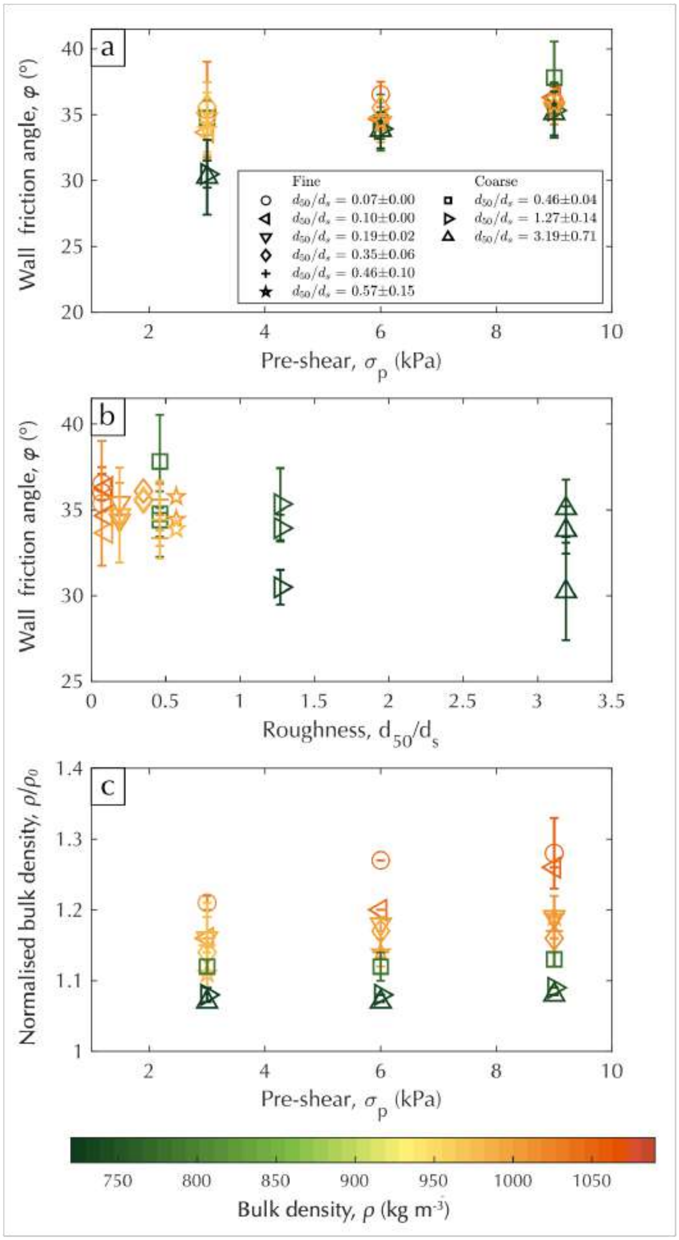

Figure 11: Bulk solid properties for the wall friction measurements. (a) Wall friction angle, φ_{wall} as a function of pre-shear normal stress, σ_p, (b) Wall friction angle, φ_{wall} as a function of roughness ratio, d_{50}/d_s, (c) Normalised bulk density, ρ/ρ_0 for the wall friction measurements. The symbols are coloured according to the bulk density of the sample, ρ consolidated at normal stress σ_p. The error bars for $d_{50}/d_s = 0.07 \pm 0.00$,$0.19 \pm 0.02$, and 0.46 ± 0.10 are zero because the measurements were performed only once.

5. Titan2D numerical simulations

In order to illustrate the importance of the internal and the wall friction angles on the dynamics of the geophysical flows, we modelled a granular flow travelling down an idealised volcanic cone. The simulations were modelled using Titan2D software (Patra et al., 2005) with a Coulomb rheology. The main input parameters for running simulations are: (1) a digital elevation model (DEM), (2) the volume of the granular flow, V, (3) the internal friction angle, φ'_{int}, and (4) the bed friction angle, φ_{bed}. As explained in the Introduction Section, the internal friction angle used in the depth-averaged models is the internal friction angle at the steady-state flow, φ_{ss}. However, in order to keep the nomenclature consistent with the Titan2D model and with the previous studies, in this section and in the related Figures 12-14, we refer to this angle as the internal friction angle, φ'_{int}. Additionally, since in the basal condition the wall friction angle is equivalent to the bed friction angle, we refer to the wall friction angle as the bed friction angle in this section. As the purpose of these simulations is to show the effects of φ'_{int} and φ_{bed} on the flow dynamics, the dimensional parameters are provided for completeness only and all the results are presented in a non-dimensional form, i.e., normalised by the initial conditions, to show relative differences.

The Digital Elevation Model (DEM) of the fictive volcano was generated by assuming that the volcano is a symmetric cone and its elevation is defined as

$$z(r) = H(1 - r^s), \tag{13}$$

where r is the radial distance from the vent normalised by the radius, R, of the volcano, H is the maximum elevation of the volcano (summit), and s is the slope factor, where $s > 1$ represents a shallower slope. The volcanic slopes were made more realistic using Perlin noise which is a technique used to produce natural appearing textures on procedurally generated terrain (Perlin, 1985). Perlin noise scale was set to $p_s = 1.0$ and three noise amplitudes were investigated: $p_a = 0.5$, corresponding to a nearly smooth DEM, $p_a = 2.5$, corresponding to vertical variations of $\pm$ 2 m (e.g., rubble-covered lava and small levees), and $p_a = 5.0$, corresponding to a very rough terrain controlling flow paths. The parameters used to generate the DEM are provided in Table 5. Three volcanoes were created of height $H = 500$ m, 785 m, and 1630 m, each having average slopes at mid-elevation of 10°, 15°, and 30°. Table 5 also

Table 5: Parameters used to generate the DEM of the three idealised volcanic cones and parameters used for Titan2D simulations.

Parameter	Value
Volcano height, H	500 m, 785 m, 1630 m
Volcano slope near crater	1°, 2°, 3°
Volcano slope at mid-elevation	10°, 15°, 30°
Volcano slope at the base	27°, 38°, 59°
Volcano radius, R	2500 m
Crater radius, r_c	250 m
Crater depth, h_c	25 m
Slope factor, s	2.5
Horizontal resolution	10 m
Terrain noise scale, p_s	1.0
Max noise amplitude, p_a	0.5, 2.5, 5.0
Height of the pile, h_0	1000 m
Radius of the pile, r_0	100 m
Flow volume, V	10^7 m^3

presents the values of the volcanic slopes near the crater, at mid-elevation, and at the base. The simulations will be referred to by the mid-elevation slope angle.

The simulations were ran assuming an initial pile of material with a height of $h_0 = 1000\,\mathrm{m}$ and a radius of $r_0 = 100\,\mathrm{m}$, giving an approximate flow volume of $V = 10^7\,\mathrm{m}^3$. The flow is simulated using a collapsing, initial stationary pile of granular material, i.e., with a zero flux source akin to a dome collapse. This means that there is no eruption/flux duration associated with the simulations and $t = 0\,\mathrm{s}$ is the start of the simulation. All the simulations were run for $t = 3600\,\mathrm{s}$. While in some simulations, the flows have not reached their final velocity after 3600 s and would have still been propagating, the aim here is to illustrate the effects of the internal and bed friction angles and not to predict the flow path and final deposit thickness. Similarly, the dimensional parameters of the volcano and the initial pile are deliberately exaggerated for sensitivity illustration.

Figure 12 shows the lateral stress coefficient, $k_{act/pass}$ calculated for all the measured angles φ'_{int} and φ_{bed}. For the diverging flow, for all values of φ_{bed}, the corresponding values of $k_{act/pass}$ indicate that the ground-normal (bed-normal) stress dominates over the ground-parallel stress (lateral stress), while the opposite is true for the converging flow. When the bed is of maximum roughness ratio, i.e., $\varphi'_{int} = \varphi_{bed}$, $k_{act/pass}$ has only one value, which means that a granular material can move down the slope with zero divergence (no thinning or thickening) only if the bed friction equals the internal friction angle (Iverson and Denlinger, 2001). Based on this analysis, the internal and bed friction angles for the simulations were chosen to be the maximum and the minimum values of φ'_{int} and φ_{bed} but with the condition that $\varphi'_{int} > \varphi_{bed}$. Additionally, we tested $\varphi_{bed} = 20°$. The Titan2D model was therefore implemented with $\varphi'_{int} = 38°$ and $48°$, and $\varphi_{bed} = 20°$, $30°$, and $37°$ (stars in Figure 12), which gives six different simulations. We will refer to the six simulations using the friction angles and the noise amplitude, e.g., a simulation with $p_a = 5$, $\varphi'_{int} = 38°$ and $\varphi_{bed} = 30°$ will be referred to as "simulation 53830".

Figure 13 presents temporal evolution of the normalised flow thickness, h/h_0 Titan2D simulations for the 10° volcano and for $p_a = 5$ for $\varphi'_{int} = 30°$, $38°$ and $\varphi_{bed} = 30°$, $37°$. At $t = 30\,\mathrm{s}$, the flow area appears to be governed by the angle of internal friction, φ'_{int} and the bed friction angle, φ_{bed}. Even though the 54830 flow area in Figure 13a is similar to the 53830 flow area in Figure 13g, the flow areas for 54837 and 53837 (Figure 13d and 13j) are noticeably different, implying that the internal friction strongly affects the flow behaviour in those cases. This can be explained by the fact that the volcanic slope is shallower around the summit and the internal friction of the granular material plays an important role in the flow dynamics. For the same volume, granular material with a greater φ'_{int} can form a flow unit inclined at a steeper angle, i.e., can form a higher (thicker) flow unit.

As the terrain slope becomes steeper, the bed friction becomes more important and the simulations begin to group according to the bed friction angle, φ_{bed}. For $t \geq 1500\,\mathrm{s}$, the 54830 flow area is comparable to the 53830 flow area (Figure 13b-c and 13e-f). Similarly, the 54837 flow area matches the 53837 flow area (Figure 13h-i and 13k-l). It is thus observed that while initially the internal friction angle has a significant impact on the flow behaviour, the bed friction becomes more important with time as the flow propagates over steeper local slopes. It is significantly easier for the material with a lower bed friction angle to flow down the slopes of the volcano.

Therefore, the flow areas for $\varphi_{bed} = 30°$ are greater than for $\varphi_{bed} = 37°$. The effects of internal friction are also still apparent with the flow areas greater for $\varphi'_{int} = 38°$, the smaller internal friction angle.

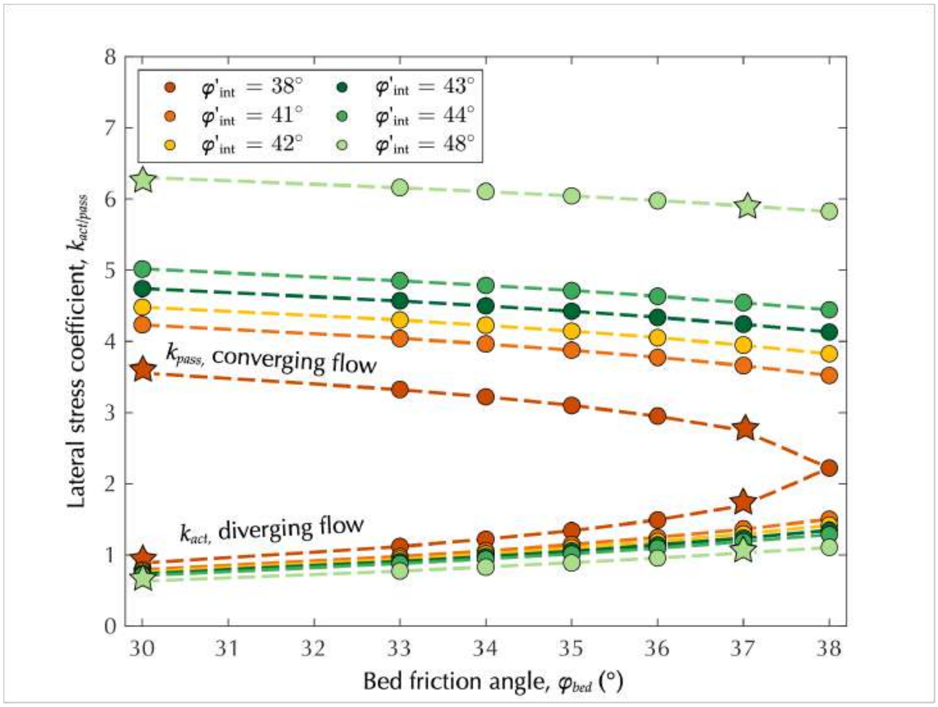

Figure 12: Lateral stress coefficient, $k_{act/pass}$ calculated using Equation 5 for the internal friction angle, φ'_{int} and the bed friction angle, φ_{bed} measured in this study. The stars correspond to the values of the angles used for the Titan2D simulations.

Quantitative relationships between the flow area and the friction angles are illustrated in Figure 14 for all the studied volcanic slopes and all the terrain noise amplitudes. Although the time varies, we observe a transition from internal-friction-dependence to bed-friction-dependence for all the simulations. The differences in the time at which this transition occurs are a direct consequence of the local slope of the volcano. For instance, the volcanic slope proximal to the crater for the 30° volcano is three times greater than for the 10° volcano, which means that the internal friction will dominate for longer for the shallower volcanic slope. It also appears that in our simulations, the noise amplitude does not affect the flow dynamics. Although we modelled and studied three idealised volcanic cones, the simulations show that regardless of the volcanic slope and the noise amplitude, the flow dynamics is governed by the angle of internal friction, φ'_{int} near the crater, while the bed friction becomes more important further away from the vent, i.e., as the volcanic slopes become steeper. Figure 14 also shows that all the flows with $\varphi_{bed} = 20°$ result in the largest flow area in the shortest time, implying great velocity and high-mobility. These results suggests that, in general, the bed friction angle might be considered as more important for modelling the flow path and runout distance of granular flows.

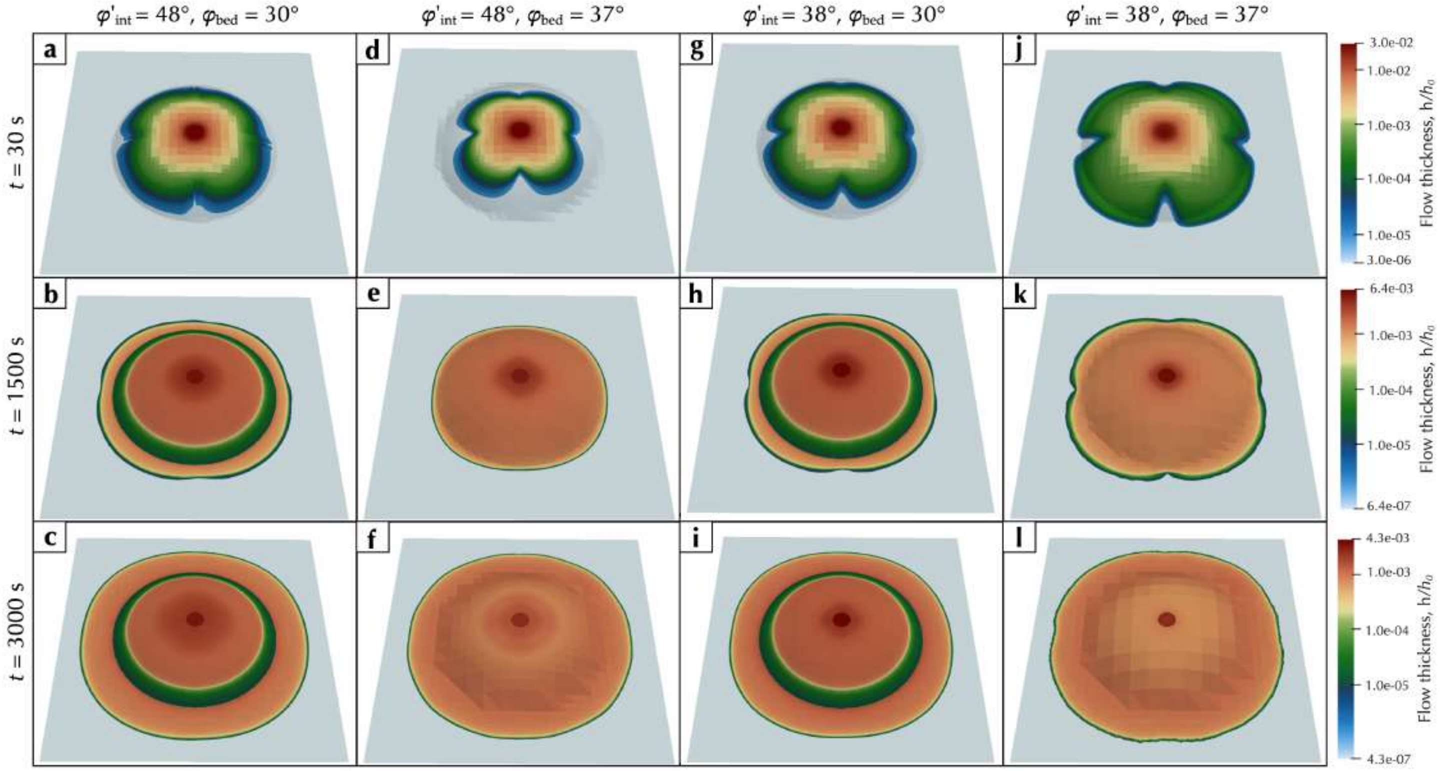

Figure 13: Titan2D simulations of a volcanic mass flowing down a 15° volcano with $p_a = 5$ showing the normalised flow thickness, h/h_0 for (a)-(c) The internal friction angle, $\varphi'_{int} = 48°$ and the bed friction angle, $\varphi_{bed} = 30°$; (d)-(f) The internal friction angle, $\varphi'_{int} = 48°$, the bed friction angle, $\varphi_{bed} = 37°$; (g)-(i) The internal friction angle, $\varphi'_{int} = 38°$, the bed friction angle, $\varphi_{bed} = 30°$; and (j)-(l) The internal friction angle, $\varphi'_{int} = 38°$, the bed friction angle, $\varphi_{bed} = 37°$. Each simulation is presented at time t =30 s (top row), $t = 1500$ s (middle row), and $t = 3000$ s (bottom row) with a corresponding colour scale for h/h_0.

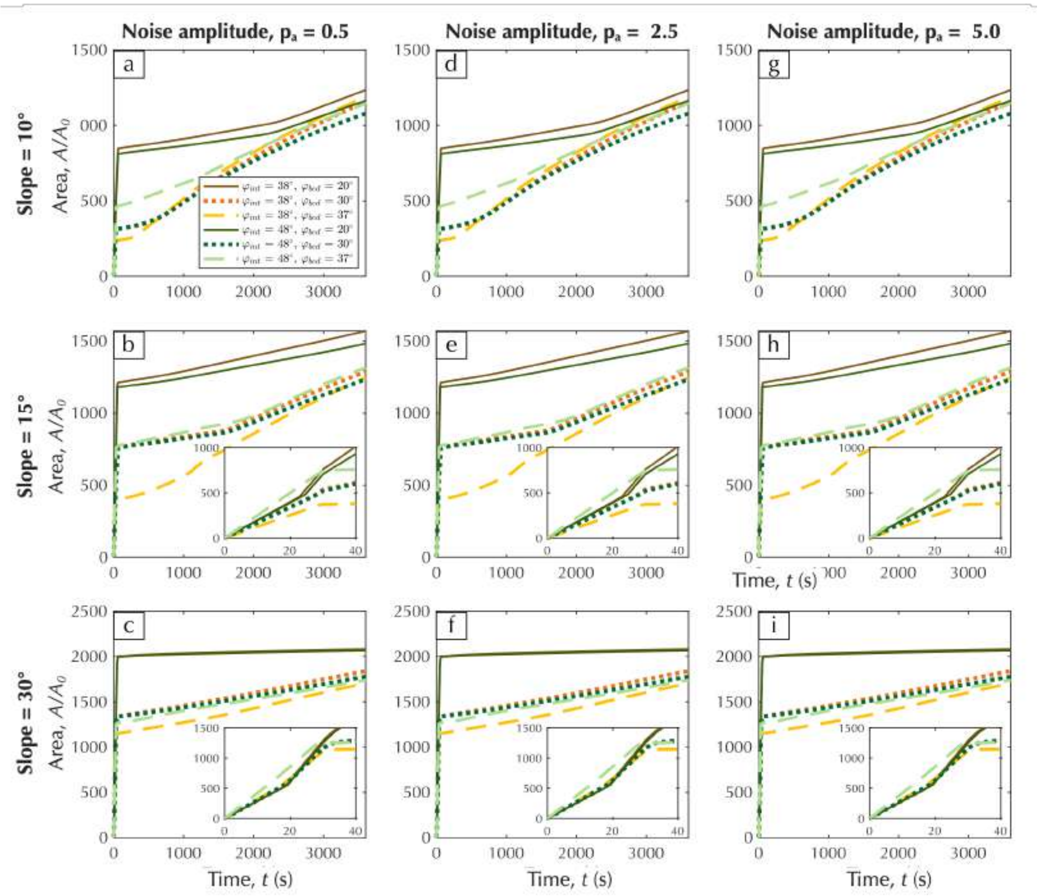

Figure 14: Temporal evolution of normalised area of the flow, A/A_0 for Titan2D simulations of a mass flowing down a volcano with a 10° slope (top row), 15° slope (middle row), and 30° slope (bottom row) for noise amplitude (a)-(c) $p_a = 0.5$, (d)-(f) $p_a = 2.5$, and (g)-(i) $p_a = 5.0$. A_0 is the area of the pile at $t = 0\,\mathrm{s}$.

6. Discussion

While this work reports measurements of frictional properties of real volcanic material, there are several limitations that need to be taken into account when interpreting the results. Firstly, we were only able to study two grain size distributions, "fine" and "coarse". Although our work provides important experimental data, they have to be extrapolated to a wider parameter space with caution. In terms of the internal friction values, our results corroborate previous studies which showed that granular material composed of smaller particles has lower values of the internal friction angles than material comprising coarse particles. For example, Prokes et al. (2024) reports that 1-1.4 mm clay particles have greater values of the angle of internal friction than particles of 0-0.5 mm diameter. Similarly, the study of Vangla and Latha (2015) shows that the angle of internal friction is smaller for sand particles of diameter 75-425 µm than for 2000-4750 µm. In our study, the wall friction angles were measured for roughness ratio $d_{50}/d_s = 0.07$ - 3.90. The statistical analysis shows that the wall friction does not depend on the roughness ratio which contradicts previous studies, at least within our studied parameter space. Jing et al. (2016) investigated friction behaviour of granular materials with roughness ratio $d_{50}/d_s = 0.4$ - 2.0 and reported that $d_{50}/d_s = 0.4$ and 0.5 leads to nonslip basal conditions, while considerable slip always occurs for $d_{50}/d_s = 2.0$. A nonslip basal condition means that a granular flow layer immediately in contact with a stationary surface has zero velocity, i.e., the surface is sufficiently rough that the flow cannot propagate without friction. The experiments of Jing et al. (2016) thus showed, that granular materials comprising particle diameters twice as big as the substrate roughness flow over these rough surfaces as if the surfaces were smooth. In our experiments, it is likely that the presence of fine material in the "coarse" mixture was sufficiently high to influence the measurements. The small particles might have filled the spaces between the sandpaper particles, changing the roughness experienced by the bulk of the granular material. Goujon et al. (2003) refers to this phenomenon as the hole-filling mechanism, where the roughness of the substrate depends on whether or not the spaces between the sand particles are filled with the granular material.

Secondly, the experiments were performed using a pre-dried material which was stored in a desiccator cabinet to avoid any moisture adsorption. We cannot fully rule out that extremely low moisture contents could have contributed to the calculated cohesion values, which are very low or zero for all the measurements. Walding et al. (2023) show that cohesion, and consequently the internal friction, increases drastically even for relatively small changes in moisture content (>0.5%). Additionally, the measurements were conducted at ambient (room temperature) and are thus focused on particle behaviour at temperatures below their glass transition temperature, T_g. High temperatures at vent proximal locations and near the base of pyroclastic density currents that support conditions $> T_g$ could lead to particle agglutination, sintering, and a marked increase in cohesion (Valentine et al., 2000; Heap et al., 2014).

Thirdly, here, the main purpose of the numerical simulations was to illustrate the impact of the studied friction angles on the dynamics of granular flows. Our simulations were performed with a symmetrical cone as a volcano which significantly simplified the simulations and resulted in symmetrical flow areas. In nature, volcanoes are rarely symmetrical and volcanic flows often favour certain slopes, resulting in more complex flow paths. Our results show that while the internal friction angle initially influences the flow, the bed friction quickly becomes more important and dominates the flow behaviour. We expect that the transition from the internal-friction-dependence to bed-friction-dependence would not occur at the same time and distance from the vent for all the flanks of the volcano with a more realistic edifice. The internal- and bed-friction-dependence finding agrees with previous research where the Titan2D simulations were shown to be nearly independent of the internal friction angle but highly sensitive to the values of the bed friction angle (e.g., Charbonnier and Gertisser, 2009; Sheridan et al., 2010; Rupp et al., 2006; Macías et al., 2008; Neglia et al., 2021). Moreover, several studies argue that in order to accurately model flow propagation over complex terrain, a spatially varying bed friction angles should be implemented (e.g., Stinton et al., 2004; Charbonnier et al., 2015; Ogburn and Calder, 2017). Additionally, although we used the experimentally determined friction angles in the numerical simulations, those values were measured during small-scale experiments where particle size, shape, and morphology all played a crucial role in the behaviour of the granular material. In particular, extra care needs to be taken when upscaling the calculated wall friction angle to the bed friction angle used in geophysical models such as Titan2D. Previous, and numerous research highlights that in order to match the simulations to the field deposits, the bed friction is often surprisingly low. For instance, Tennant et al. (2021) found that a basal friction angle of $\varphi_{bed} = 6°$ was required to reproduce lithic-rich PDCs at Gede volcano, Indonesia. A low value was also required for accurate modelling the Mixcun block and ash flow at the Tacana Volcanic complex, Mexico-Guatemala ($\varphi_{bed} = 7°$) and the 2010 PDCs at Soufrière Hills, Montserrat ($\varphi_{bed} = 7°$) (Vázquez et al., 2019; Ogburn and Calder, 2017).

Finally, pyroclastic density currents are highly mobile granular flows capable of travelling tens to hundreds of kilometres on slopes of only a few degrees (Wilson, 1980; Sparks et al., 1978; Dufek, 2016). Their mobility is often attributed to gas–particle interactions and pore-pressure effects that promote partial fluidisation (e.g., Delannay et al., 2017; Lube et al., 2019). PDCs are typically density-stratified, with a concentrated basal region underlying a more dilute turbulent ash cloud (Sulpizio et al., 2014; Dufek, 2016; Lube et al., 2020; Jones et al., 2023). However, the basal concentrated layer is not necessarily dominated by coarse particles; rather, its rheology is governed by an effective grain-size scale such as the Sauter mean diameter, d_{32}, which is strongly controlled by polydispersity and fine-particle content (Breard et al., 2019). As a result, even apparent "coarse" PDCs with millimetre-scale median grain sizes (d_{50}) may exhibit much smaller dynamically relevant length scales. The particle size distribution in natural PDCs spans from micron-sized ash to metre-scale clasts, but the experiments presented here focus on particles with diameters <710 µm and without imposed fluidisation. These conditions are therefore most representative of the dense, sheared basal regions where compaction, shear at the bed, and suppression of fluidisation are expected (Druitt et al., 2004; Bareschino et al., 2007; Lipiejko and Jones, 2024). Importantly, this does not diminish the relevance of the measurements: continuum two-phase and mixture-theory frameworks increasingly couple dry granular rheology with pore-pressure diffusion, enabling laboratory-derived constitutive behaviour to be incorporated directly into models that account for transient fluidisation. In this context, the experimental findings provided here offer valuable input for such closures, particularly in regimes where effective stress, compaction, and shear-dependent permeability control the evolution of excess pore pressure and mobility.

7. Conclusions

This contribution reports an experimental investigation into the internal and the wall friction angles of pyroclastic material. We studied two granular material mixes: "fine" with particles of diameters $0\,\mu m < d < 180\,\mu m$ and $d_{50} = 25 \pm 1\,\mu m$, and "coarse", with particles of diameters $d < 710\,\mu m$ and $d_{50} = 170 \pm 13\,\mu m$. The internal friction angles were measured for pre-shear normal (i.e., consolidating) stresses, σ_p = 1.5-9 kPa and the wall friction angle was measured for σ_p = 1.5-9 kPa against a range of sandpapers with particle diameters 42 µm- 380 µm. The studied particle to sand particle ratio, i.e., the roughness was d_{50}/d_s = 0.07 - 3.90. The effects of the friction angles on the dynamics of a granular flows was discussed through a series of Titan2D (depth-averaged model) numerical simulations. The simulations involved granular flows with the bed friction angle, $\varphi_{bed} = 20°$, 30°, and 37°, and the internal friction angle, $\varphi'_{int} = 38°$ and 48°, travelling down an idealised volcanic cone with slopes inclined at 10°, 15°, and 30°. The key findings of this study are as follows.

1. For the range of studied particle sizes, coarse material has greater angles of internal friction than the fine material, suggesting that fine material is more susceptible to flowing for a given applied force.
2. The studied consolidating normal stress, $\sigma_p = 1.5\text{-}9\,\text{kPa}$, which controls the bulk density of the material, has an insignificant effect on the internal friction angles.
3. In our experiments, the particle size to the sandpaper particle size ratio, i.e., roughness, $d_{50}/d_s = 0.07$ - 3.90, do not impact the wall friction angles.
4. The numerical simulations show that, for all the studied volcanic slopes (10° - 30°), the internal friction governs the flow dynamics around the volcanic crater, while the bed friction dominates regions further away from the vent.
5. This study provides an experimental data set of the measurements of frictional properties of pyroclastic material of diameters $0\,\mu\text{m} < d < 180\,\mu\text{m}$ with $d_{50} = 25 \pm 1\,\mu\text{m}$, and $d < 710\,\mu\text{m}$ with $d_{50} = 170 \pm 13\,\mu\text{m}$ for consolidating stress, $\sigma_p = 1.5\text{-}9\,\text{kPa}$.

Data Availability

Data supporting the findings of this study are openly available at https://doi.org/10.5281/zenodo.17122990.

Acknowledgments

We would like to acknowledge the Natural Environment Research Council (NERC) who funded this research (Grant reference number: NE/W006286/1). TJJ was also supported by a UK Research and Innovation (UKRI) Future Leaders Fellowship (Grant reference number: MR/W009781/1). JP was supported by a scholarship of the German Academic Exchange Service (DAAD;

Grant reference number: GB_ES_PH_0159). We would also like to acknowledge two anonymous reviewers whose comments improved the clarity and quality of the manuscript.

References

S. B. Savage, K. Hutter, Acta Mechanica The dynamics of avalanches of granular materials from initiation to runout. Part I: Analysis, Acta Meechanica 86 (1991) 201–223.

R. M. Iverson, R. P. Denlinger, Flow of variably fluidized granular masses across three-dimensional terrain: 1. Coulomb mixture theory, Journal of Geophysical Research: Solid Earth 106 (2001) 537–552. doi:10.1029/2000jb900329.

S. Dartevelle, Numerical modeling of geophysical granular flows: 1. A comprehensive approach to granular rheologies and geophysical multiphase flows, Geochemistry, Geophysics, Geosystems 5 (2004). doi:10.1029/2003GC000636.

K. Hutter, Geophysical granular and particle-laden flows: review of the field, Philosophical Transactions of the Royal Society A: Mathematical, Physical and Engineering Sciences 363 (2005) 1497–1505. doi:10.1098/rsta.2005.1591.

Y. Forterre, O. Pouliquen, Flows of dense granular media, Annual Review of Fluid Mechanics 40 (2008) 1–24. doi:10.1146/annurev.fluid.40.111406.102142.

R. Delannay, A. Valance, A. Mangeney, O. Roche, P. Richard, Granular and particle-laden flows: From laboratory experiments to field observations, Journal of Physics D: Applied Physics 50 (2017). doi:10.1088/1361-6463/50/5/053001.

G. Lube, E. C. P. Breard, T. Esposti-Ongaro, J. Dufek, B. Brand, Multiphase flow behaviour and hazard prediction of pyroclastic density currents, Nature Reviews Earth & Environment 1 (2020) 348–365. doi:10.1038/s43017-020-0064-8.

T. J. Jones, F. Beckett, B. Bernard, E. C. P. Breard, F. Dioguardi, J. Dufek, S. Engwell, J. Eychenne, Physical properties of pyroclastic density currents: relevance, challenges and future directions, Frontiers in Earth Science Volume 11 - 2023 (2023). doi:10.3389/feart.2023.1218645.

C. Coulomb, Essai sur une application des regles de maximis et minimis quelques problemes de statique, relatits a l'architecture, Memoires de Mathematique de l'Academie Royale de Science 7, Paris (1776).

K. Kelfoun, T. H. Druitt, Numerical modeling of the emplacement of Socompa rock avalanche, Chile, Journal of Geophysical Research: Solid Earth 110 (2005). doi:10.1029/2005JB003758.

A. K. Patra, A. C. Bauer, C. C. Nichita, E. B. Pitman, M. F. Sheridan, M. Bursik, B. Rupp, A. Webber, A. J. Stinton, L. M. Namikawa, C. S. Renschler, Parallel adaptive numerical simulation of dry avalanches over natural terrain, Journal of Volcanology and Geothermal Research 139 (2005) 1–21. doi:10.1016/j.jvolgeores.2004.06.014.

R. M. Iverson, D. L. George, A depth-averaged debris-flow model that includes the effects of evolving dilatancy. I. Physical basis, Proceedings of the Royal Society A: Mathematical, Physical and Engineering Sciences 470 (2014) 20130819. doi:10.1098/rspa.2013.0819.

M. de' Michieli Vitturi, T. Esposti Ongaro, G. Lari, A. Aravena, IMEX_SfloW2D 1.0: a depth-averaged numerical flow model for pyroclastic avalanches, Geoscientific Model Development 12 (2019) 581–595. doi:10.5194/gmd-12-581-2019.

M. de' Michieli Vitturi, T. Esposti Ongaro, S. Engwell, IMEX_SfloW2D v2: a depth-averaged numerical flow model for volcanic gas–particle flows over complex topographies and water, Geoscientific Model Development 16 (2023) 6309–6336. doi:10.5194/gmd-16-6309-2023.

R. Williams, A. J. Stinton, M. F. Sheridan, Evaluation of the Titan2D two-phase flow model using an actual event: Case study of the 2005 Vazcún Valley Lahar, Journal of Volcanology and Geothermal Research 177 (2008) 760 – 766. doi:10.1016/j.jvolgeores.2008.01.045.

J. N. Procter, S. J. Cronin, T. Platz, A. Patra, K. Dalbey, M. Sheridan, V. Neall, Mapping block-and-ash flow hazards based on Titan 2D simulations: a case study from Mt. Taranaki, NZ, Natural Hazards 53 (2010) 483–501. doi:10.1007/s11069-009-9440-x.

M. F. Sheridan, A. K. Patra, K. Dalbey, B. Hubbard, Probabilistic digital hazard maps for avalanches and massive pyroclastic flows using TITAN2D, in: G. Groppelli, L. Viereck-Goette (Eds.), Stratigraphy and Geology of Volcanic Areas, Geological Society of America, 2010, p. 0. doi:10.1130/2010.2464(14).

N. Alcozer-Vargas, M.-P. Reyes-Hardy, A. Esquivel, F. Aguilera, A GIS-based multi-hazard assessment at the San Pedro volcano, Central Andes, northern Chile, Frontiers in Earth Science Volume 10 - 2022 (2022). doi:10.3389/feart.2022.897315.

R. Azzaro, S. D'Amico, T. Esposti Ongaro, G. Ganci, A. Garcia, S. Scollo, M. Aliotta, B. Behncke, A. Bevilacqua, G. Bilotta, S. Branca, C. Cassisi, M. Coltelli, P. Del Carlo, M. de' Michieli Vitturi, A. Di Roberto, L. Lodato, L. Mereu, M. Prestifilippo, C. Proietti, L. Sandri, T. Tuvè, F. Zuccarello, A. Cappello, Towards a Multi-Hazard Assessment at Etna Volcano (Italy): The PANACEA Project, in: A. Malheiro, F. Fernandes, H. I. Chaminé (Eds.), Advances in Natural Hazards and Volcanic Risks: Shaping a Sustainable Future, Springer Nature Switzerland, Cham, 2023, pp. 31–35.

E. Aydar, P. Labazuy, C. Diker, Scenario-based hazard assessment of Mt Hasan Stratovolcano, Central Anatolia, Türkiye, Bulletin of Volcanology 87 (2025) 37. doi:10.1007/s00445-025-01818-z.

K. F. E. Cui, G. G. D. Zhou, T. Man, Y. Huang, Y. Zhang, X. Lu, T. Zhao, Modeling the Dense Granular Flow Rheology of Particles With Different Surface Friction: Implications for Geophysical Mass Flows, Journal of Geophysical Research: Earth Surface 130 (2025) e2024JF008048. doi:10.1029/2024JF008048.

R. M. Nedderman, Statics and Kinematics of Granular Materials, Cambridge University Press, 1992. doi:10.1017/CBO9780511600043.

R. W. Whorlow, Rheological techniques, Ellis Horwood, New York, 1992.

H. M. Mader, E. W. Llewellin, S. P. Mueller, The rheology of two-phase magmas: A review and analysis, 2013. doi:10.1016/j.jvolgeores.2013.02.014.

O. Pouliquen, Powders and cohesive granular media: a rheological perspective, Rheologica Acta 64 (2025) 195–207. doi:10.1007/s00397-025-01490-2.

A. W. Jenike, R. T. Shield, On the Plastic Flow of Coulomb Solids Beyond Original Failure, Journal of Applied Mechanics 26 (1959) 599–602. doi:10.1115/1.4012119.

A. W. Jenike, Storage and flow of solids. Bulletin No. 123 of the Utah Engineering Experiment Station; Vol. 53, No. 26, Technical Report, Utah Univ., Salt Lake City (United States), 1976. doi:10.2172/5240257.

D. Schulze, Flow Properties of Powders and Bulk Solids (2014).

ASTM International, Test Method for Shear Testing of Powders Using the Freeman Technology FT4 Powder Rheometer Shear Cell, 2015. doi:10.1520/D7891-15.

N. I. Deligne, D. Mckay, R. M. Conrey, G. E. Grant, E. R. Johnson, J. O'Connor, K. Sweeney, U. S. G. Survey, Field-trip guide to mafic volcanism of the Cascade Range in Central Oregon—A volcanic, tectonic, hydrologic, and geomorphic journey, Technical Report, Reston, VA, 2017. doi:10.3133/sir20175022H.

P. A. Webb, C. Orr, M. I. Corporation, Analytical Methods in Fine Particle Technology, Micromeritics Instrument Corporation, 1997.

T. G. Mezger, The Rheology Handbook, 4th ed., Vincentz Network, Hannover, Germany, 2012. doi:10.1515/9783748600367.

ANSI, Specifications for the Size of Abrasive Grain - Grinding Wheels, Polishing and General Uses. American National Standard Institute B74.12-2018, 2018.

The MathWorks Inc., MATLAB version: 9.13.0 (R2022b), 2022.

B. Cagnoli, M. Manga, Granular mass flows and Coulomb's friction in shear cell experiments: Implications for geophysical flows, Journal of Geophysical Research: Earth Surface 109 (2004). doi:10.1029/2004jf000177.

J. Samuelson, C. Marone, B. Voight, D. Elsworth, Laboratory investigation of the frictional behavior of granular volcanic material, Journal of Volcanology and Geothermal Research 173 (2008) 265–279. doi:10.1016/j.jvolgeores.2008.01.015.

P. Vangla, G. M. Latha, Influence of Particle Size on the Friction and Interfacial Shear Strength of Sands of Similar Morphology, International Journal of Geosynthetics and Ground Engineering 1 (2015). doi:10.1007/s40891-014-0008-9.

H. Shi, R. Mohanty, S. Chakravarty, R. Cabiscol, M. Morgeneyer, H. Zetzener, J. Ooi, A. Kwade, S. Luding, V. Magnanimo, Effect of Particle Size and Cohesion on Powder Yielding and Flow, KONA Powder and Particle Journal 2018 (2018). doi:10.14356/kona.2018014.

C. P. Doncaster, A. J. H. Davey, Analysis of Variance and Covariance: How to Choose and Construct Models for the Life Sciences, Cambridge University Press, 2007.

K. Perlin, An image synthesizer, in: Proceedings of the 12th Annual Conference on Computer Graphics and Interactive Techniques, SIGGRAPH '85, Association for Computing Machinery, New York, NY, USA, 1985, pp. 287–296. doi:10.1145/325334.325247.

R. Prokes, L. Jezerska, D. Gelnar, J. Zegzulka, M. Zidek, Internal friction and flowability of clay powder depend on particle moisture, size and normal stress, Powder Technology 446 (2024) 120184. doi:10.1016/j.powtec.2024.120184.

L. Jing, C. Y. Kwok, Y. F. Leung, Y. D. Sobral, Characterization of base roughness for granular chute flows, Physical Review E 94 (2016) 52901. doi:10.1103/PhysRevE.94.052901.

C. Goujon, N. Thomas, B. Dalloz-Dubrujeaud, Monodisperse dry granular flows oninclined planes: Role of roughness, The European Physical Journal E 11 (2003) 147–157. doi:10.1140/epje/i2003-10012-0.

N. Walding, R. Williams, P. Rowley, N. Dowey, Cohesional behaviours in pyroclastic material and the implications for deposit architecture, Bulletin of Volcanology 85 (2023) 67. doi:10.1007/s00445-023-01682-9.

G. A. Valentine, F. V. Perry, G. WoldeGabriel, Field characteristics of deposits from spatter-rich pyroclastic density currents at Summer Coon volcano, Colorado, Journal of Volcanology and Geothermal Research 104 (2000) 187–199. doi:10.1016/S0377-0273(00)00206-7.

M. J. Heap, S. Kolzenburg, J. K. Russell, M. E. Campbell, J. Welles, J. I. Farquharson, A. Ryan, Conditions and timescales for welding block-and-ash flow deposits, Journal of Volcanology and Geothermal Research 289 (2014) 202–209. doi:10.1016/j.jvolgeores.2014.11.010.

S. J. Charbonnier, R. Gertisser, Numerical simulations of block-and-ash flows using the Titan2D flow model: examples from the 2006 eruption of Merapi Volcano, Java, Indonesia, Bulletin of Volcanology 71 (2009) 953–959. doi:10.1007/s00445-009-0299-1.

B. Rupp, M. Bursik, L. Namikawa, A. Webb, A. K. Patra, R. Saucedo, J. Luis Macias, C. Renschler, Computational modeling of the 1991 block and ash flows at Colima Volcano, Mexico, in: C. Siebe, J. L. Macías-Gerardo, J. Aguirre-Díaz (Eds.), Neogene-Quaternary Continental Margin Volcanism: A perspective from Mexico, Geological Society of America, 2006, p. 0. doi:10.1130/2006.2402(11).

J. L. Macías, L. Capra, J. L. Arce, J. M. Espíndola, A. García-Palomo, M. F. Sheridan, Hazard map of El Chichón volcano, Chiapas, México: Constraints posed by eruptive history and computer simulations, Journal of Volcanology and Geothermal Research 175 (2008) 444–458. doi:10.1016/j.jvolgeores.2008.02.023.

F. Neglia, R. Sulpizio, F. Dioguardi, L. Capra, D. Sarocchi, Shallow-water models for volcanic granular flows: A review of strengths and weaknesses of TITAN2D and FLO2D numerical codes, Journal of Volcanology and Geothermal Research 410 (2021) 107146. doi:10.1016/j.jvolgeores.2020.107146.

A. J. Stinton, M. Sheridan, A. Patra, K. Dalbey, L. Namikawa, Integrating variable bed friction into the TITAN2D mass-flow model: applications to the Little Tahoma Peak Avalanches, Acta Vulcanol 16 (2004) 153–163.

S. J. Charbonnier, J. L. Palma, S. Ogburn, Revista geologica de America Central, Revista Geológica de América Central (2015) 107–128.

S. E. Ogburn, E. S. Calder, The Relative Effectiveness of Empirical and Physical Models for Simulating the Dense Undercurrent of Pyroclastic Flows under Different Emplacement Conditions, Frontiers in Earth Science Volume 5 - 2017 (2017). doi:10.3389/feart.2017.00083.

E. Tennant, S. F. Jenkins, A. Winson, C. Widiwijayanti, H. Gunawan, N. Haerani, N. Kartadinata, W. Banggur, H. Triastuti, Reconstructing eruptions at a data limited volcano: A case study at Gede (West Java), Journal of Volcanology and Geothermal Research 418 (2021) 107325. doi:10.1016/j.jvolgeores.2021.107325.

R. Vázquez, J. L. Macías, J. L. Arce, G. Cisneros, R. Saucedo, Numerical simulation of block-and-ash flows for different eruptive scenarios of the Tacaná Volcanic Complex, México-Guatemala, Journal of Volcanology and Geothermal Research 373 (2019) 36–50. doi:10.1016/j.jvolgeores.2019.01.026.

C. J. N. Wilson, The role of fluidization in the emplacement of pyroclastic claws: An experimental approach, Journal of Volcanology and Geothermal Research 8 (1980) 231–249. doi:10.1016/0377-0273(80)90106-7.

R. S. J. Sparks, L. Wilson, G. Hulme, Theoretical modeling of the generation, movement, and emplacement of pyroclastic flows by column collapse, Journal of Geophysical Research: Solid Earth 83 (1978) 1727–1739. doi:10.1029/JB083IB04P01727.

J. Dufek, The Fluid Mechanics of Pyroclastic Density Currents, Annual Review of Fluid Mechanics 48 (2016) 459–485. doi:10.1146/annurev-fluid-122414-034252.

G. Lube, E. C. P. Breard, J. Jones, L. Fullard, J. Dufek, S. J. Cronin, T. Wang, Generation of air lubrication within pyroclastic density currents, Nature Geoscience 12 (2019) 381–386. doi:10.1038/S41561-019-0338-2.

R. Sulpizio, P. Dellino, D. M. Doronzo, D. Sarocchi, Pyroclastic density currents: state of the art and perspectives, Journal of Volcanology and Geothermal Research 283 (2014) 36–65. doi:10.1016/j.jvolgeores.2014.06.014.

E. C. Breard, J. R. Jones, L. Fullard, G. Lube, C. Davies, J. Dufek, The Permeability of Volcanic Mixtures—Implications for Pyroclastic Currents, Journal of Geophysical Research: Solid Earth 124 (2019) 1343–1360. doi:10.1029/2018JB016544.

T. H. Druitt, G. Bruni, P. Lettieri, J. G. Yates, The fluidization behaviour of ignimbrite at high temperature and with mechanical agitation, Geophysical Research Letters 31 (2004). doi:10.1029/2003GL018593.

P. Bareschino, T. Gravina, L. Lirer, A. Marzocchella, P. Petrosino, P. Salatino, Fluidization and de-aeration of pyroclastic mixtures: The influence of fines content, polydispersity and shear flow, Journal of Volcanology and Geothermal Research 164 (2007) 284–292. doi:10.1016/j.jvolgeores.2007.05.013.

N. Lipiejko, T. J. Jones, Permeability of granular mixtures under shear, Powder Technology 444 (2024) 120064. doi:10.1016/j.powtec.2024.120064.